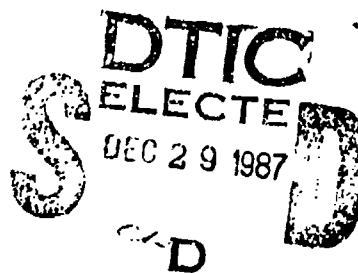AFWAL-TR-87-4086

AD-A189 524

NONDESTRUCTIVE EVALUATION OF CARBON-CARBON COATINGS

D.C. Copley
GE Aircraft Engines
1 Neumann Way
Cincinnati, Ohio 45215

M. Rooney
Southern Research Institute
Birmingham, Alabama

DTIC
ELECTE
DEC 2 9 1987
D

October 1987

Final Report for Period August 1984 - February 1987

MATERIALS LABORATORY
AIR FORCE WRIGHT AERONAUTICAL LABORATORIES
AIR FORCE SYSTEMS COMMAND
WRIGHT-PATTERSON AIR FORCE BASE, OHIO 45433-6563

REPORT DOCUMENTATION PAGE

1a. REPORT SECURITY CLASSIFICATION	1b. RESTRICTIVE MARKINGS
UNCLASSIFIED	

2a. SECURITY CLASSIFICATION AUTHORITY	3. DISTRIBUTION/AVAILABILITY OF REPORT
	Approved for Public Release; Distribution Unlimited.
2b. DECLASSIFICATION/DOWNGRADING SCHEDULE	

4. PERFORMING ORGANIZATION REPORT NUMBER(S)	5. MONITORING ORGANIZATION REPORT NUMBER(S)
	AFWAL-TR-87-4086

6a. NAME OF PERFORMING ORGANIZATION	6b. OFFICE SYMBOL (If applicable)	7a. NAME OF MONITORING ORGANIZATION
General Electric Company Aircraft Engine Business Group		Air Force Wright Aeronautical Laboratories Materials Laboratory (AFWAL, MLLP)

6c. ADDRESS (City, State, and ZIP Code)	7b. ADDRESS (City, State and ZIP Code)
PO Box 156301 1 Neumann Way Cincinnati, OH 45215-6301	Wright-Patterson Air Force Base Dayton, OH 45433-6563

8a. NAME OF FUNDING/SPONSORING ORGANIZATION	8b. OFFICE SYMBOL (If applicable)	9. PROCUREMENT INSTRUMENT IDENTIFICATION NUMBER
		F33615-84-C-5007

8c. ADDRESS (City, State and ZIP Code)	10. SOURCE OF FUNDING NOS.			
	PROGRAM ELEMENT NO.	PROJECT NO.	TASK NO.	WORK UNIT NO.
	62102F	2418	02	23

11. TITLE (Include Security Classification)
Nondestructive Evaluation of C-C Coating

12. PERSONAL AUTHOR(S)
D.C. Copley (GE); M. Rooney (Southern Research Institute, Birmingham, Alabama)

13a. TYPE OF REPORT	13b. TIME COVERED	14. DATE OF REPORT (Yr., Mo., Day)	15. PAGE COUNT
Final	FROM 8/1/84 TO 2/23/87	October 1987	94

16. SUPPLEMENTARY NOTATION

17 COSATI CODES			18. SUBJECT TERMS (Continue on reverse if necessary and identify by block number)
FIELD	GROUP	SUB GR	
11	03		Nondestructive Testing, Carbon-Carbon, Coatings, Differential Absorption, Finite-Element Modeling
	06		

19. ABSTRACT (Continue on reverse if necessary by block number)

General Electric, with Southern Research Institute as subcontractor, completed this program to investigate differential-absorption, nondestructive evaluation for carbon-carbon coatings. An optimum fluorescent particle and application method were developed to visualize crack patterns in the coatings. A stress-analysis model was developed to predict crack spacing as a function of coating properties, and this provided excellent agreement with experimental results. A study was made of the potential to improve oxidation life by adding glass-formers to the fluorescent particle suspension. A number of methods for measurement of coating thickness were investigated, and eddy current measurement was found to be the most accurate.

20. DISTRIBUTION AVAILABILITY OF ABSTRACT	21. ABSTRACT SECURITY CLASSIFICATION
UNCLASSIFIED-UNLIMITED ☒ SAME AS RPT ☐ DTIC USERS ☐	UNCLASSIFIED

22a. NAME OF RESPONSIBLE INDIVIDUAL	22b. TELEPHONE NUMBER (Include Area Code)	22c. OFFICE SYMBOL
C. Buynak	513-255-9807	AFWAL/MLLP

DD FORM 1473, 83 APR   EDITION OF 1 JAN 73 IS OBSOLETE

TABLE OF CONTENTS

TABLE OF CONTENTS (Concluded)

LIST OF ILLUSTRATIONS

LIST OF ILLUSTRATIONS (Continued)

LIST OF ILLUSTRATIONS (Concluded)

LIST OF TABLES

1.0 INTRODUCTION

1.1 OBJECTIVES

The goals of this program were to develop the differential-absorption nondestructive evaluation (NDE) technique for characterization of corrosion-initiating cracks in the oxidation-protective coating on carbon-carbon (C-C) turbine components and to investigate the potential of using a modification of this NDE technique to improve the oxidation resistance of the coating.

1.2 BACKGROUND

Carbon-carbon materials are being developed for high-temperature use in gas turbine engines and other applications. Useful C-C properties include high specific strength and stiffness at elevated temperature as well as thermal-shock resistance. One of the major obstacles to the use of C-C is oxidation at high temperatures. Resistance to oxidation can be improved by the use of external coatings and by matrix oxidation inhibitors. Most coating systems are multilayered and involve conversion of the outer carbon-carbon layers to silicon carbide, followed in some cases by the addition of more silicon carbide to produce a hard outer layer. Glass-forming materials are also added to the coating with the intention of producing a viscous glass at elevated temperatures in order to seal cracks and pores. This program was conducted primarily on materials, manufactured by LTV Corporation, consisting of noninhibited carbon-carbon substrate and a silicon carbide conversion coating with outer sealant layer.

The coating layers have a higher coefficient of thermal expansion than the carbon-carbon substrates, and this mismatch induces tensile thermal stresses during component cooldown. Regular crazing patterns in the coatings result from these thermal stresses. The thermally induced cracks are a normal feature of the coated composite. At high temperatures, cracks should be closed due to thermal expansion, and the coating will then provide protection. Glass-forming compounds in the coating protect the substrate in the inter-mediate range where oxidation may still occur but where the cracks are not fully closed.

Nondestructive evaluation of coating quality had proved to be difficult using traditional NDE methods. Reasons included the variable density and porosity of the coating and the irregular surface finish caused by the coating process. Another difficulty was the lack of knowledge about what coating features were critical to performance.

The differential absorption method had been suggested as potentially useful for detection and characterization of coating cracks. This method uses a fluorescent dye in an alcohol carrier fluid that wets the surface of the coating. The greater absorption of the material in the vicinity of a crack means that the dye particles are deposited at this type of flaw, thus making the crack highly visible on the surface of the component. The development of

1

this method formed the basis of the program. One goal was to determine the best combination of dye material, fluid carrier, and application technique.

The detection of cracks is not itself an indicator of coating quality. However, the presence of a normal or abnormal crack pattern may provide useful information. The formation of a crazing pattern during cooldown is a function of local stress states and may be influenced by defects and discontinuities.

One approach pursued in this program was to see if the effectiveness of the coating could be improved by using the differential-absorption method to add glass-forming compounds to the coating. This would have the advantage of a highly localized application in which the materials are concentrated at the crack sites.

A number of other nondestructive evaluation techniques were investigated in addition to differential absorption. These were eddy current, film and computerized tomography (CT) radiography, beta backscatter, ultrasonics, and thermography. The objective was to assess the usefulness of these methods to characterize both uncoated and coated carbon-carbon materials.

1.3 CONCLUSIONS

A formulation and method of application were developed for differential absorption. The use of powdered dye was improved by microencapsulation of the dye particles. This was an extremely valuable way to control particle size and substantially improved crack visibility.

The method was generally successful in imaging crack patterns in LTV's Type I Mod I coating on LTV's ACCRP and K650 substrates.

The visibility of the surface-crack pattern was highly variable and was strongly affected by the background intensity. This depended on coating surface finish which is in turn affected by the thermal and environmental history of the coated part. Cracks were usually more visible on thermally cycled coatings.

Cracks form a regular crazing pattern with principal directions parallel to the warp and fill directions of the substrate yarn weave. The most useful and easily measured feature of the pattern was crack spacing.

A mathematical model was developed to study the coating cool-down process and resulting crack formation. This was expressed as an analytical (shear-lag) approach and as a more detailed finite-element model. Crack patterns predicted were in agreement with those observed on the samples. Crack spacing varied with coating/substrate thickness ratio as predicted by the model.

The results of oxidation tests did not show any clear effect of added sealants on oxidation life. Three sealant formulations were used; however, none showed a clear improvement over untreated samples.

Coating crack patterns showed some changes after extensive oxidation. The cracks increased greatly in visibility. The resulting crack patterns sometimes indicated major delamination under the coating; however, the crack pattern was not a reliable indicator of oxidation damage from one cycle.

CT radiography and eddy current tests both give reliable indication of oxidation damage, but CT radiography provides the most complete and direct indication. However, both methods may have limitations in testing materials with inhibited-matrix substrate.

Ultrasonic and CT radiography tests were able to detect delaminations in uncoated, noninhibited carbon-carbon. CT radiography was also sensitive to internal variations in density.

Various methods were investigated for measurement of coating thickness. Of these, the most accurate results were produced by eddy current testing. Beta backscatter and CT radiography also gave useful indication of coating thickness but were less accurate than the eddy current measurement.

2.0 SUMMARY OF APPROACH

2.1 TASK I - SPECIMEN PREPARATION AND CHARACTERIZATION

Plates of uncoated carbon-carbon material were obtained and characterized by radiographic and ultrasonic NDE methods. The plates were cut into 3×1×0.25 inch coupons that were also characterized extensively.

The specimens were coated by LTV using multiple runs to introduce a wide variation in coating parameters. Defects and contamination were deliberately introduced. The coated coupons were examined by film radiography, CT radiography, thermography, eddy current, and beta backscatter. The results were recorded for correlation with later metallographic testing.

2.2 TASK II - TECHNIQUE OPTIMIZATION AND CHARACTERIZATION

Coefficients of thermal expansion were measured on substrate, coating, and coated coupons. A number of coupons were subjected to thermal cycling, and the resultant cracks were studied to evaluate size and morphology. A microencapsulation method was developed to control dye particle size and concentration. Numerous dye formulations, microcapsule sizes, and carrier fluids were evaluated, and a process was selected for this application.

The formation of cracks in the coating was modeled mathematically, and a computer program was written to predict crack spacing by means of either an analytical or a finite-element model. Properties of the coating and substrate were measured to provide input to the model.

Three possible crack-healing additives were formulated and applied to a selection of test coupons. Oxidation tests were carried out on these coupons and on control samples to evaluate the effect of the additives. Performance was monitored by weight-loss measurements and subsequent NDE.

2.3 TASK III - METHOD DEMONSTRATION

Cracks were generated in the remaining coated coupons by heat treatment. The coupons were then subjected to the differential-absorption test, and the results were photographed and documented. Twenty specimens were sectioned, polished, examined, and photographed. Coating thickness was measured from the photographs and correlated with previous NDE measurements. Coupons made from two additional substrate/coating systems were examined by CT radiography and differential absorption, and the results were documented.

2.4 PROGRAM ORGANIZATION

The prime contractor for this program was the GE Aircraft Engine Business Group, Evendale, Ohio. A major portion of the effort was performed under

4

subcontract by Southern Research Institute (SoRI), Birmingham, Alabama. The main SoRI responsibilities were thermal and physical characterization of materials and the development of the dye microencapsulation and application processes.

3.0 SPECIMEN PREPARATION AND CHARACTERIZATION

The objective of this task was to produce coupons of coated carbon-carbon material for use in the later development and evaluation of the differential-absorption method. It was necessary to induce a selection of defects and variations in the coupons in order to evaluate the method fully. The approach was to perform thorough nondestructive and thermophysical characterization of material at all stages. LTV Corporation expended considerable effort and ingenuity in providing the materials and producing the necessary defects. It must be emphasized that the anomalous material was supplied specifically at GE request and is not representative of production-quality material.

3.1 CARBON-CARBON PLATES

Two plates of warp-aligned carbon-carbon material were obtained from LTV. One of these plates was K650 material; the other was ACCRP. Plate dimensions were 20×10×0.25 in.

Ultrasonic through-transmission tests were performed on the plates. The plate of K650 showed through-transmission attenuation varying from 6 to 28 dB at 2.25 MHz. Figure 1 shows the ultrasonic C-Scan print-outs. The ACCRP showed attenuation between 18 and >80 dB. The areas of very high attenuation corresponded to apparent delaminations where the material surface could be deformed by finger pressure. These suspected delaminations were positively identified as such on subsequent plate cut-up. Pulse-echo attenuation and time-of-flight measurements made by SoRI gave excellent agreement with the through-transmission test results, and over many areas the delamination interface was located by an echo. The more minor variations in attenuation were not accounted for.

The plates were cut into 3×1 inch coupons according to the plan shown in Figure 2. The intention was to produce coupons aligned in the warp, fill, and 45° directions. Also included in the cutup plan was the production of 12 specimens for coefficient of thermal expansion (CTE) measurement. These were 3×0.5×0.25 inch and consisted of two coupons of each material in each of the warp, fill, and 45° orientations. A number of the ACCRP coupons split along the delamination planes during cutting. The areas of this delamination were identical with the areas identified in the C-scan recording.

3.2 UNCOATED TEST COUPONS

The uncoated test coupons were physically marked by corner grinding to indicate serial number and orientation as shown in Figure 3. The dimensions of the coupons were recorded, and the specimens were dried and weighed. This information was used to calculate initial density and for comparison to values generated after specimen coating. The initial density values allowed for the missing corner volumes mentioned above. Tables 1 and 2 list the physical dimensions, weights, and calculated densities obtained.

20 dB Through 60 dB
in This Area

80% at 23 dB

80% at 25 dB

80% at 20 dB

30 dB Through Total
Sound Attenuation
in This Area

80% at 17 dB

Transducer Frequency Used 2.25 MHz 0.375 in. Dia
(Flat) Threshold Level 4 dB Thickness 0.275 in.
10/26/84

(a) ACCRP Material

80% at 28 dB

80% at 6 dB

80% at 25 dB

82% at 22 dB

Transducer Frequency 2.25 MHz 0.375 in. Dia (Flat)
Threshold Level - 4 dB Thickness 0.263 in.
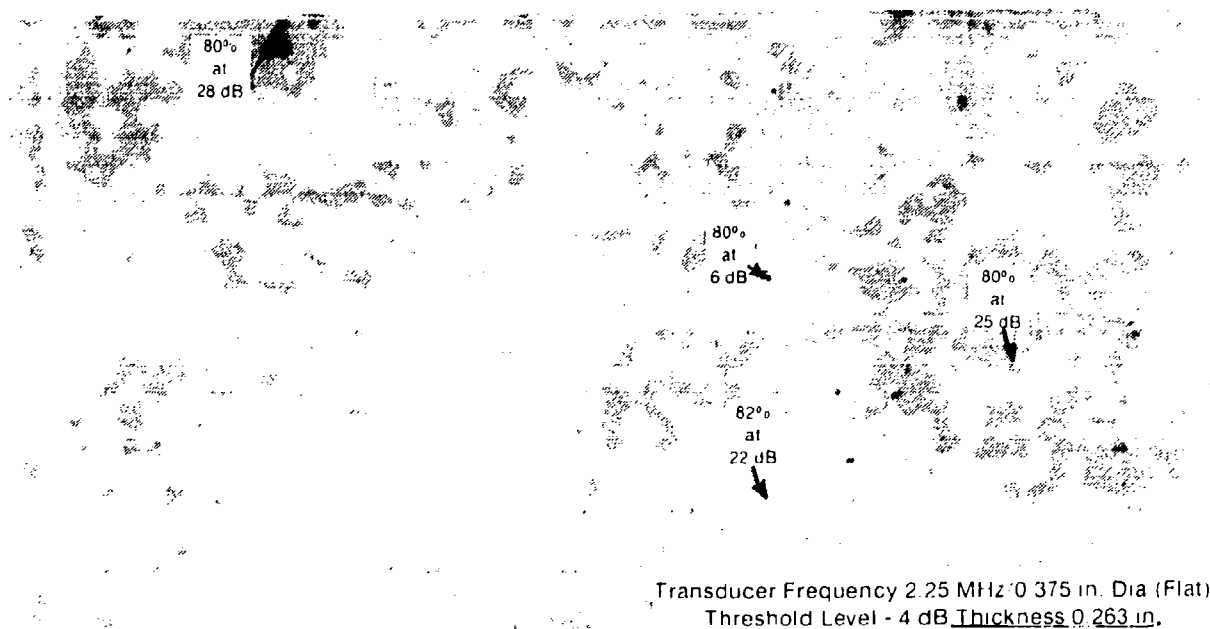
(b) K650 Material

Figure 1. Ultrasonic Through-Transmission C-Scans of Plate Material.

7
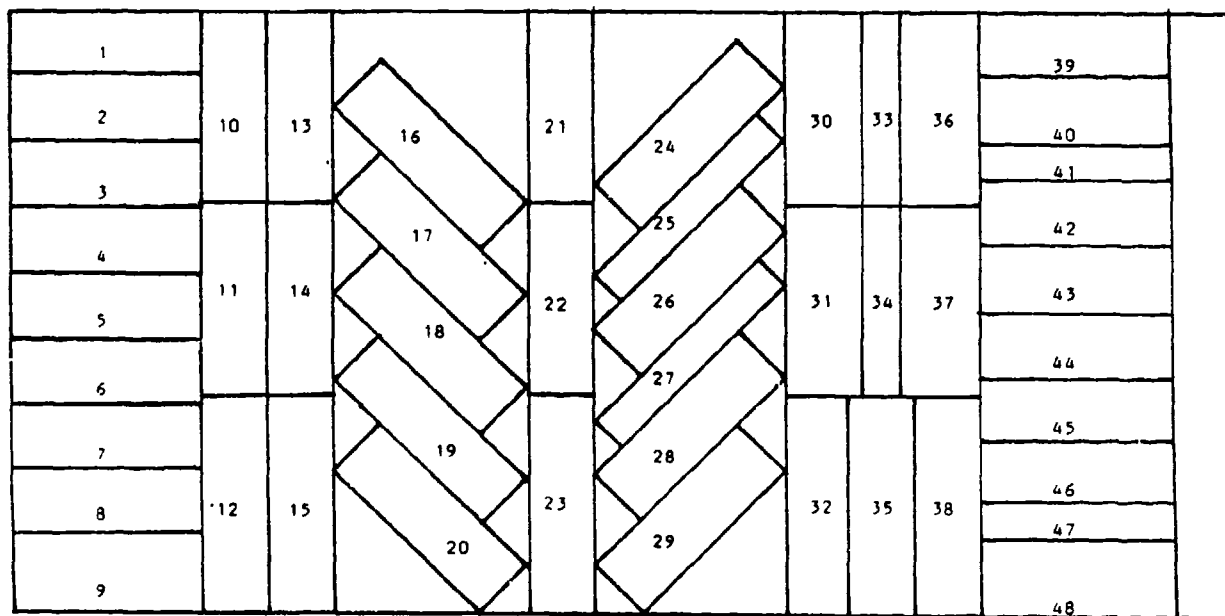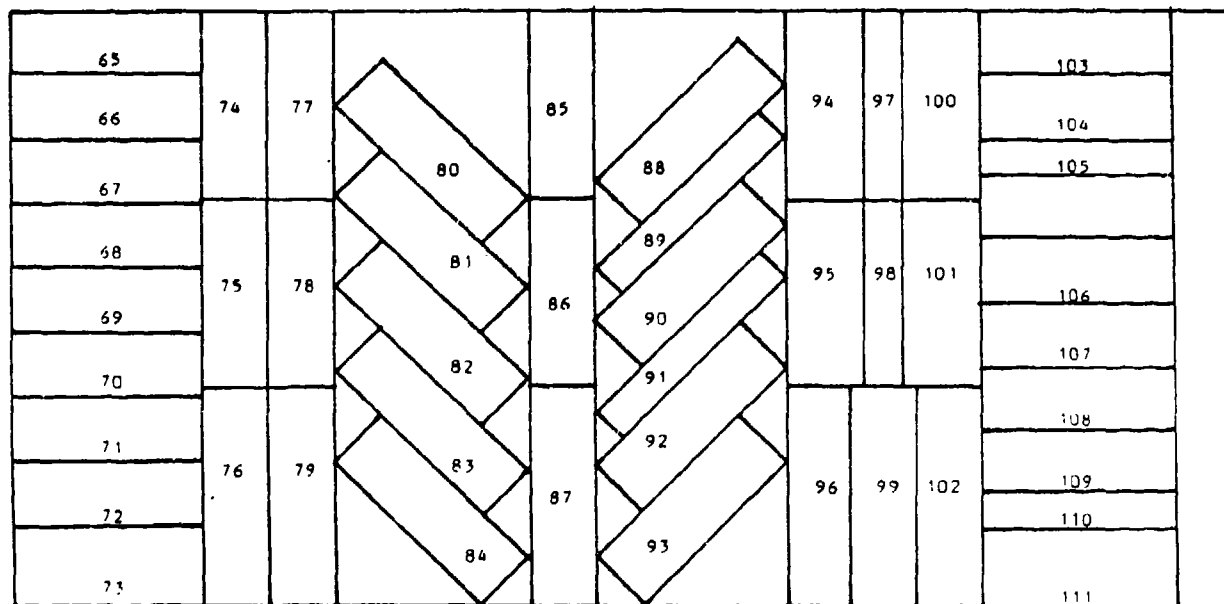
(a) ACCRP Material

(b) K650 Material

Figure 2. Carbon-Carbon Plate Cup-up Plan.

8
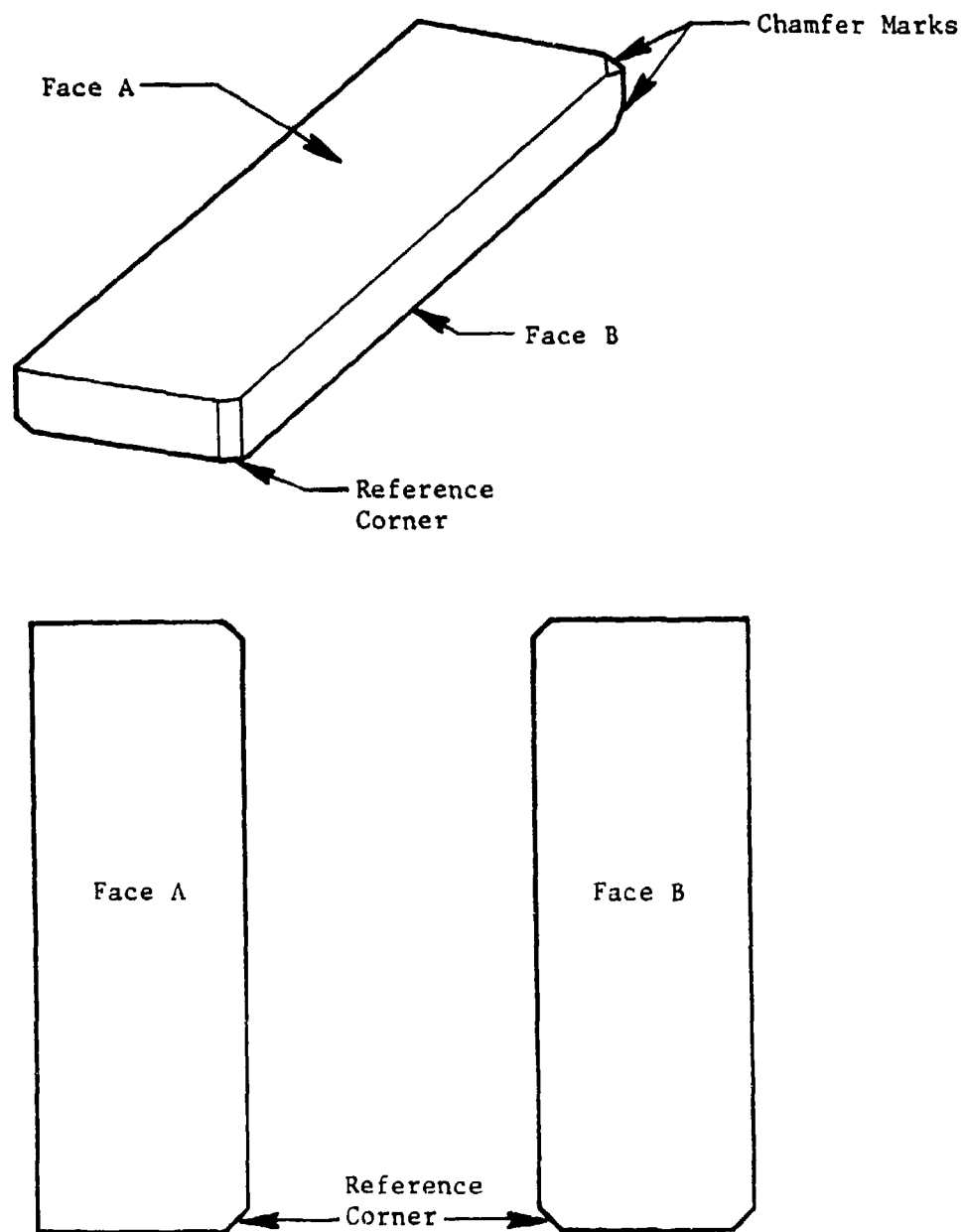
Figure 3.   Specimen Identification and Corner
            Marking.

Table 1. Specimen Densities for Coated and Uncoated ACCRP 2D C-C Material.

Specimen	Dimensions (in.): Uncoated			Coated			Weights (gm):		Density (g/cc):	
	Height	Width	Length	Height	Width	Length	Uncoated	Coated	Uncoated	Coated
ACCRP-1	0.2643	1.0010	3.111	0.2686	1.0047	3.121	21.8662	23.0840	1.6239	1.6751
-2	0.2610	1.0278	3.109	0.2658	1.0308	3.118	22.2733	23.5357	1.6324	1.6639
-3	0.2613	1.0279	3.107	0.2694	1.0318	3.118	22.3063	23.7132	1.636-	1.6743
-8	0.2643	1.0292	3.106				22.3600		1.6375	N/A
-9	0.2632	1.0283	3.106	0.2781	1.0316	3.115	22.3685	24.1390	1.6290	1.6617
-10	0.2638	1.0287	3.131	0.2746	1.0313	3.137	22.5255	25.7716	1.6230	1.7767
-13	0.2629	1.0130	3.134	0.2803	1.0161	3.140	22.1668	25.5751	1.6296	1.7571
-16	0.2599	1.0136	3.057	0.2683	1.0165	3.063	21.4527	24.3676	1.6233	1.7331
-17	0.2617	1.0129	3.054	0.2833	1.0154	3.057	21.4145	25.1748	1.6196	1.7612
-21	0.2638	1.0258	3.186	0.2893	1.0275	3.190	22.6411	25.7583	1.6121	1.7234
-22	0.2600	1.0247	3.186	0.2757	1.0303	3.194	22.5768	26.4937	1.6333	1.8068
-23	0.2612	1.0275	3.186	0.2857	1.0326	3.196	22.6172	27.6103	1.6213	1.7947
-24	0.2607	1.0109	3.055	0.2673	1.0135	3.060	21.3149	24.5412	1.6210	1.8079
-25				0.2718	0.5274	3.161		13.4470	N/A	1.8155
-26	0.2607	1.0367	3.053	0.2675	1.0405	3.061	21.9485	25.1362	1.6255	1.8119
-28	0.2614	1.0523	3.057	0.2675	1.0593	3.065	22.2583	25.3681	1.6273	1.7901
-29	0.2600	1.0532	3.058	0.2669	1.0582	3.072	22.1975	25.3309	1.6291	1.7528
-32	0.2598	1.0633	3.179	0.2659	1.0691	3.191	23.3254	26.4360	1.6233	1.7815
-33				0.2728	0.5388	3.196		14.1104	N/A	1.8074
-35	0.2594	1.0111	3.185	0.2665	1.0163	3.202	22.1622	25.2432	1.6260	1.7841
-38	0.2607	0.9862	3.185	0.2671	0.9952	3.191	21.6673	24.7004	1.6277	1.7656
-39	0.2653	1.0130	3.193	0.2768	1.0181	3.198	22.3074	26.2039	1.6029	1.7756
-40	0.2605	1.0132	3.184	0.2729	1.0172	3.194	22.1015	25.4165	1.6118	1.8077
-41				0.2739	0.5234	3.218		13.3925	N/A	1.8422
-42	0.2607	1.0362	3.184	0.2700	1.0395	3.191	22.6505	26.3572	1.6146	1.8041
-43	0.2606	1.0374	3.192	0.2700	1.0421	3.190	22.6900	26.6278	1.6157	1.8037
-44	0.2608	1.0394	3.182	0.2781	1.0424	3.188	22.6997	26.4031	1.6151	1.7735
-45	0.2601	1.0378	3.181	0.2678	1.0425	3.192	22.7002	26.5316	1.6225	1.8038
-47	0.2595	1.0123	3.185	0.2695	1.0177	3.194	22.3902	25.3981	1.6143	1.8157
-48	0.2607	1.0094	3.185	0.2674	1.0132	3.191	21.9025	25.1304	1.6298	1.7771

							Average (g/cc)		1.6216	1.7781
							Standard Deviation (g/cc)		0.0094	0.0507
							Coefficient of Variation %		0.58	2.77

Table 2. Specimen Densities for Coated and Uncoated K650 2D C-C Material.

	Dimensions (in.)						Weights (gm)		Density (g/cc)	
	Uncoated			Coated						
Specimen	Height	Width	Length	Height	Width	Length	Uncoated	Coated	Uncoated	Coated
K650-65	0.2673	1.0707	3.151	0.2709	1.0732	3.157	23.0569	25.5300	1.5663	1.7071
-66	0.2687	1.0705	3.137	0.2723	1.0722	3.142	23.1502	25.7855	1.5716	1.7212
-67	0.2699	1.0696	3.151	0.2734	1.0735	3.158	23.3760	26.1438	1.5771	1.7212
-68	0.2651	1.0625	3.118				22.5617		1.5775	N.A
-69	0.2635	1.0708	3.099	0.2657	1.0732	3.106	22.4344	25.0475	1.5752	1.7296
-70	0.2688	1.0706	3.154	0.2727	1.0725	3.162	23.2091	26.0140	1.5707	1.7077
-71	0.2664	1.0692	3.124	0.2693	1.0744	3.133	22.8228	25.4504	1.5774	1.7246
-72	0.2638	1.0730	3.095				22.3551		1.5633	N.A
-73	0.2640	1.0226	3.077				21.1551		1.5625	N.A
-74	0.2695	1.0840	3.178	0.2711	1.0857	3.197	23.6657	24.7356	1.5641	1.5174
-75	0.2678	1.0798	3.171	0.2700	1.0830	3.179	23.5168	24.6650	1.5767	1.5312
-76	0.2633	1.0720	3.165	0.2658	1.0783	3.175	22.9689	24.0257	1.5721	1.5744
-77	0.2697	1.0152	3.177	0.2734	1.0178	3.180	22.2195	25.1070	1.5775	1.7512
-78	0.2676	1.0167	3.169				22.1849		1.5629	N.A
-79	0.2631	1.0121	3.172	0.2687	1.0167	3.181	21.6509	24.6208	1.5973	1.7462
-90	0.2691	1.0675	3.028	0.2731	1.0702	3.034	22.2904	25.3067	1.5700	1.7482
-91	0.2697	1.0676	3.029	0.2734	1.0700	3.035	22.3692	25.3712	1.5752	1.7541
-92	0.2672	1.0679	3.030	0.2708	1.0721	3.033	22.1752	24.3999	1.5746	1.7765
-93	0.2636	1.0675	3.024	0.2677	1.0720	3.034	21.8726	24.5099	1.5914	1.7315
-94	0.2615	1.0652	2.997	0.2657	1.0697	3.002	21.4787	24.3214	1.5752	1.7521
-95	0.2684	1.0109	3.162	0.2712	1.0122	3.164	22.0036	24.7344	1.5773	1.7517
-96	0.2671	1.0040	3.154	0.2719	1.0077	3.164	21.7572	24.3033	1.5621	1.7715
-98	0.2694	1.0268	3.027	0.2785	1.0315	3.032	21.5349	24.9263	1.5720	1.7427
-99				0.2718	0.6246	3.038		14.6574	N.A	1.7615
-90	0.2679	1.0330	3.026	0.2712	1.0360	3.033	21.5299	24.1043	1.5519	1.7415
-92	0.2627	1.0644	3.026	0.2658	1.0689	3.036	21.8151	24.1072	1.5561	1.7002
-93	0.2614	1.0630	3.026	0.2645	1.0676	3.037	21.5120	23.7977	1.5774	1.7039
-96	0.2617	1.0702	3.447				24.8742		1.5775	N.A
-97				0.2737	0.4810	3.247		12.4227	N.A	1.7782
-99	0.2619	1.0711	3.456	0.2659	1.0746	3.467	24.7492	27.4755	1.5617	1.7362
-102	0.2637	0.9762	3.454	0.2664	0.9802	3.463	22.3212	25.3777	1.5735	1.7139
-104	0.2634	1.0716	3.474				25.2257		1.5762	N.A
-107	0.2635	1.0734	3.539	0.2652	1.0762	3.516	25.3682	28.2000	1.5735	1.7175
-109	0.2588	1.0731	3.514				25.1653		1.5622	N.A
-110a				0.2519	0.5290	3.546		14.2539	N.A	1.7762
-111	0.2598	1.0265	3.543	0.2630	1.0312	3.549	23.6529	26.3979	1.5607	1.7172

			Uncoated	Coated
Average (g/cc)			1.5754	1.7315
Standard Deviation (g/cc)			0.0055	0.0245
Coefficient of Variation (%)			0.75	1.55

Ultrasonic Velocity - Measurements were made in the three principal directions on each coupon by SoRI. Tables 3 and 4 list the results. The ACCRP specimens show a higher sound velocity in-plane and a lower velocity across-ply compared with K650. This was indicative of the elastic-property differences; the ACCRP is stiffer in-plane and softer in the across-ply direction than K650.

Eddy Current - Impedance measurements were made at six locations on each sample using a Nortec NuT 25L instrument and a 0.5-inch-diameter, shielded, ferrite-core coil operated at 100 kHz frequency. The purpose was to obtain data that would later be used in eddy current estimates of coating thickness. It was believed that variations in substrate electrical conductivity could cause errors in thickness measurement, and the substrate measurements were made to preclude this.

Film Radiography - Conventional film X-radiography was performed by SoRI on the uncoated test coupons, and Figure 4 shows the results for Coupons 24 and 76. Note that the figure is a direct print from the radiograph, so tones are reversed from those seen on the film.

CT Radiography - The uncoated coupons were inspected using a GE CT9800 system at GE Medical Systems, Milwaukee. The specimens were radiographed in two stacks of approximately 40 specimens each. A tomographic scan was made at three locations along the specimen length; a typical CT cross-sectional image is shown in Figure 5. A measurement was also made of the average CT number over the cross section of each specimen. The following observations were made from the CT results:

1. Delaminations in the ACCRP specimens were observable as low CT numbers. No such regions were seen in the K650.

2. K650 specimens showed generally a lower CT number (typically 370 - 390) than the ACCRP (390 - 410). This is consistent with the fact that the ACCRP coupons had a higher average density. However, the ACCRP typically showed a lower CT number at mid-thickness; the K650 were more uniform. It is likely that the more rapid ACCRP manufacturing process resulted in a density gradient from face to center. Figure 5b shows CT number plots through the thickness of two typical specimens. Note that CT numbers are quoted on the Hounsfield scale: water has a CT number of 0, and voids have a number of -1024. Prior work (Reference 1) has identified a correlation between CT number and density for carbon-carbon and a number of other materials. Such a correlation was not evident here, probably because the range of densities was small (1.563 to 1.636).

3. A number of reconstruction artifacts were observed. There was streaking, apparently caused by the alignment of gaps between specimens, and CT number was lower than expected for specimens in the top row of the stack.

12

Table 3. Ultrasonic Velocities for ACCRP Specimens.

Specimen	Warp Uncoated	Coated	Fill Uncoated	Coated	Off-axis Uncoated	Coated	Across-ply Uncoated	Coated
ACCRP-1	0.3639	0.3806					0.0986	0.0711
-2	0.3636	0.3807					0.0946	0.0755
-3	0.3647	0.3812					0.0865	0.0735
-8	0.3658						0.0858	
-9	0.3637	0.3776					0.0914	UTR
-10			0.3603	0.3789			0.0910	0.0755
-13			0.3549	0.3756			0.0985	0.0650
-16					0.2658	0.2747	0.0922	0.0780
-17					0.2624	0.2749	0.0906	UTR
-21			0.3564	0.3718			0.0829	0.1219
-22			0.3641	0.3780			0.0932	0.0757
-23			0.3600	0.3721			0.0901	0.0962
-24					0.2585	0.2645	0.0931	0.0591
-25						0.2704		0.1387
-26					0.2621	0.2664	0.0915	0.0711
-28					0.2638	0.2766	0.0901	0.0715
-29					0.2625	0.2715	0.0903	0.0896
-32			0.3592	0.3817			0.0935	0.0713
-33				0.3800				0.1779
-35			0.3633	0.3794			0.0901	0.0718
-38	0.3634	0.3803					0.0924	0.0718
-39	0.3663	0.3834					0.0949	0.0826
-40	0.3689	0.3758					0.0940	0.0944
-41		0.3777						0.1591
-42	0.3689	0.3799					0.0919	0.0733
-43	0.3674	0.3820					0.0931	0.0774
-44	0.3687	0.3897					0.0931	0.0775
-45	0.3699	0.3814					0.0897	0.0525
-47	0.3681	0.3839					0.0958	0.0733
-48	0.3686	0.3840					0.0959	0.0777
Average	0.3665	0.3813	0.3597	0.3772	0.2625	0.2713	0.0915	0.0773
S.D.	0.0023	0.0033	0.0031	0.0034	0.0022	0.0042	0.0036	0.0096
C.O.V.	0.63	0.86	0.86	0.91	0.84	1.55	3.91	11.20

Notes: 1. 2.4MHz signal used

2. Velocities measured using first break energies

3. UTR -- Unable To Read

4. Excluded from statistics. ITE Specimens were ~0.5 inches wide -- ultrasonic paths appear to be primarily down the coating material.

13

Table 4. Ultrasonic Velocities for K650 Specimens.

Specimen	Warp Uncoated	Warp Coated	Fill Uncoated	Fill Coated	Off-axis Uncoated	Off-axis Coated	Across Uncoated	Across Coated
K650-65	0.3317	0.3395					0.1152	0.1050
-66	0.3355	0.3393					0.1041	0.3994
-67	0.3388	0.3392					0.1093	0.1005
-68	0.3333						0.1069	
-69	0.3311	0.3383					0.1054	0.3991
-70	0.3352	0.3387					0.1067	0.1073
-71	0.3352	0.3380					0.1074	0.09-6
-72	0.3339						0.1086	
-73	0.3316						0.1091	
-74			0.3153	0.3222			0.1053	0.3613
-75			0.3213	0.3241			0.1041	0.3936
-76			0.3230	0.3349			0.1045	3.0--
-77			0.3209	0.3202			0.1045	0.1005
-78			0.3172				0.10--	
-79			0.3247	0.3406			0.109-	0...3-
-80					0.2740	0.2778	0.1061	0.121-
-81					0.2708	0.2727	0.1075	0.105-
-82					0.2665	0.2715	0.1060	0..27-
-83					0.2655	0.2547	0.10--	0....
-84					0.2509	0.2631	0.10--	2.1046
-85			0.3191	0.3215			2.113-	0.10--
-86			0.3255	0.3238			2.1---	0...3-
-88					0.3137	0.3139	2.1127	0.309-
-89						0.2958		0..3--
-90					0.3072	0.2908	0.111-	-..-4-
-92					0.2684	0.2770	0.109-	2.09--
-93					0.2729	0.2746	0.1250	-.---
-96			0.3267				0.110-	
-97				0.3110				-.---
-99			0.3279	0.3340			3.1---	3..2--
-102			0.3274	0.3339			3.1---	0...3-
-104	0.3413						3.1---	
-107	0.3417	0.3397					3.1---	2.0---
-108	0.3435						2.1---	
-110a		3.3403						2..---
-111	0.3327	0.3413					3.1---	3..--
Average	0.3350	0.3394	0.3226	0.3286	0.2691	0.2690	0.10--	0..00-
S.D.	0.0041	0.0009	0.0041	0.0085	0.0176	0.0142	0.007-	0..04-
C.V.	1.23	0.29	1.26	0.59	6.3-	5.29	2.-4	4.--

Notes:
1. 0.4MHz signal used
2. Velocities measured using first break energies
3. Excluded from statistics. CTE Specimens were ~0.5 inches wide -- ultrasonic paths appear to be primarily down the coating material..

14

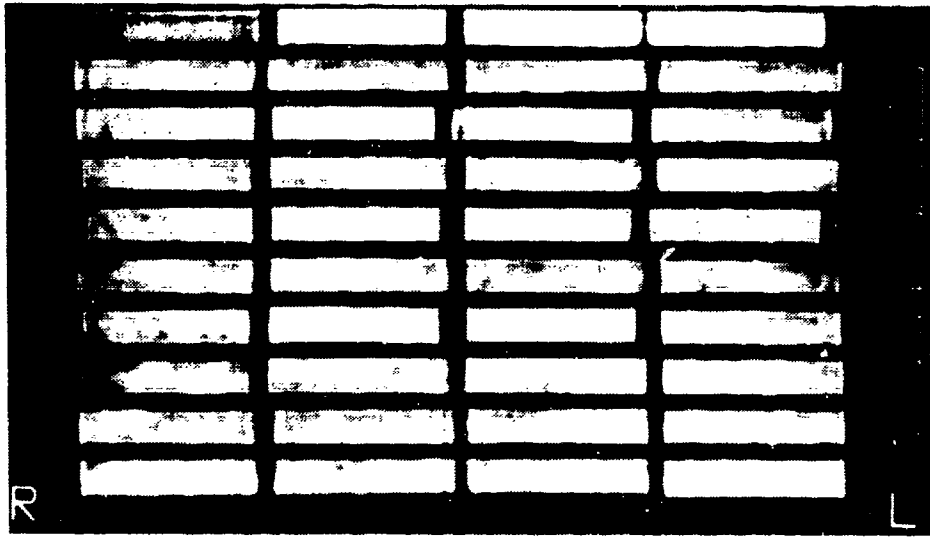Uncoated   SiC Coated

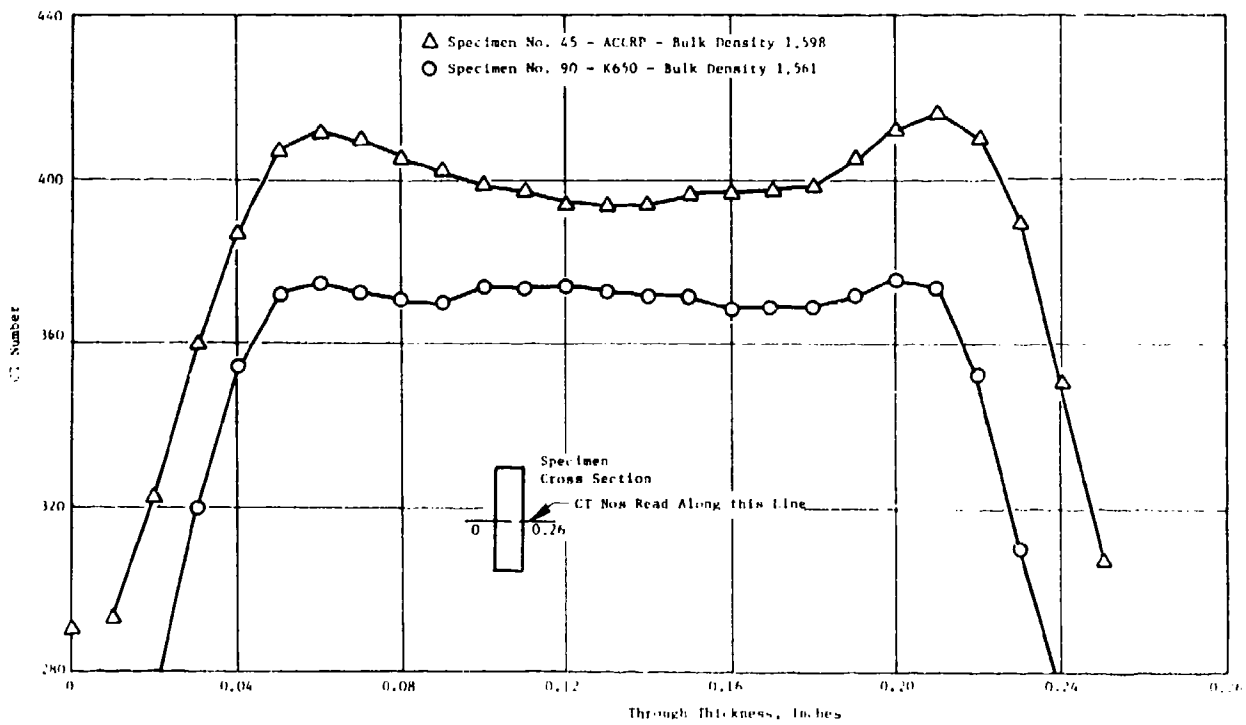(a) Specimen K650-76

Uncoated   SiC Coated
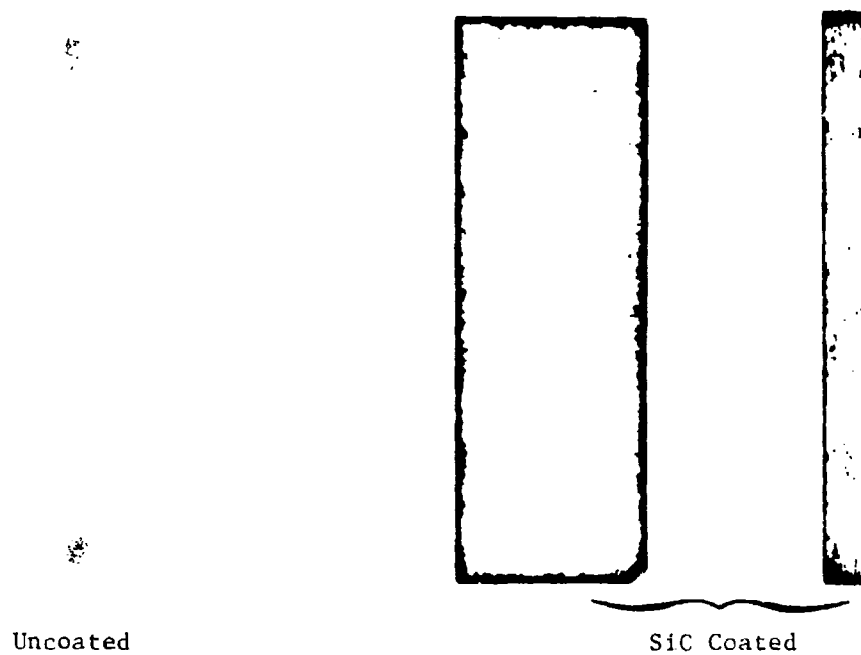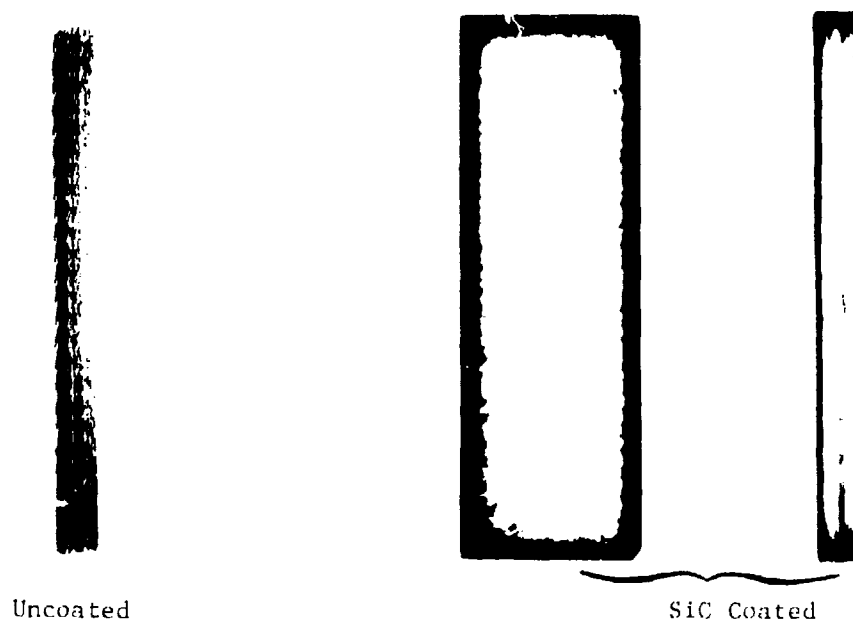
(b) Specimen ACCRP-24 Showing Delamination

Figure 4. Film Radiograph of 2D C-C Coupons.

(a) X-ray CT Cross Section of Coupon Stack

(b) CT Numbers Through Specimens 45 and 90

Figure 5. X-ray CT Scans of Uncoated Specimens.

16

<u>Thermal Expansion</u> - Six uncoated coupons were tested: three coupons representing the warp, fill, and 45° off-axis direction from each plate. The tests were performed to 3000° F using quartz and graphite dilatometry. Figure 6 shows the results. Only one line is drawn for each uncoated material (ACCRP and K650) since no differences were measured for the three fiber orientations. Note that the K650 material exhibits slightly higher thermal expansion; this may be due to processing differences that cause the K650 to be less graphitic.

3.3 COATING OF TEST COUPONS

Fifty-eight of the coupons were coated by LTV using their Type I Mod I coating process. The coated specimens consisted of 6 CTE coupons and 52 standard size.

LTV were requested to introduce variations and defects into the coating process. They accomplished this by coating the specimens in six batches using different coating parameters for each batch. Variations and defects induced during coating were grease dots, silicon metal contamination, aluminum pen marks, release agent, and short coating cycles. A full listing of the coupons and coating variations is shown in Tables 5 and 6. LTV also provided coating-thickness estimates based on eddy current measurements; these are listed in Tables 7 and 8.

The physical properties of the coating material needed to be established for the analysis described in Section 6. Coating density and coefficient of thermal expansion were experimentally determined. Accepted values of elastic modulus, Poisson's ratio, and allowable strain were estimated in consultation with scientists familiar with these materials. These values were as follows:

Density	2.59 g/cm^3
Modulus of Elasticity (E)	30.0 Msi
Poisson's Ratio	0.19
Coefficient of Thermal Expansion	2.8×10^{-6} in/in-° F
Allowable Strain	0.0067 in/in

Density measurements were made using a Micromeritics Model 1303 helium/ air pycnometer. Powder samples of the coating material were obtained by grinding the remnants of the coating thermal expansion specimens with mortar and pestle; samples from both ACCRP and K650 coupons were used. Results were confirmed by a successive grinding technique.

The thermal expansion measurements were made on specimens derived from coupons ACCRP-21 and K650-79. These coupons were sliced down the middle and heat treated at 1500° F in air until all the carbon-carbon substrate material had completely oxidized. Figure 6 shows the coating thermal expansion results of these tests. Note that the K650 coating material exhibits a higher thermal expansion than the ACCRP; this was expected because the coating material was primarily created from the substrate by a conversion technique.
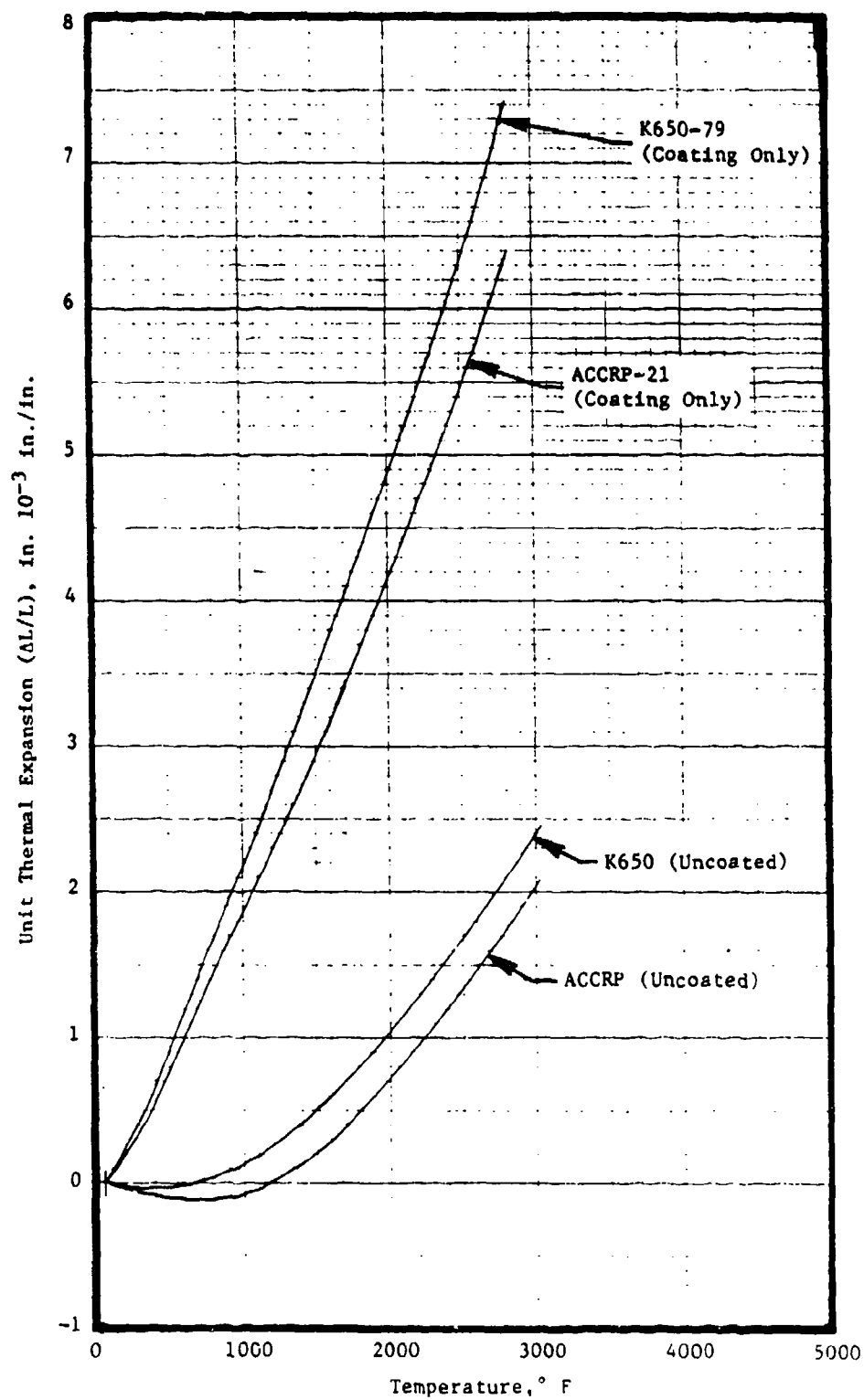
17

Figure 6.   Thermal Expansion Results From the Uncoated 2D
C-C and LTV Silicon Carbide Coating Materials.

18

Table 5. Coating Process Information for K650 Specimens.

Specimen	Coating Run	Defects/Sample Preparation (Normal Unless Noted)
ACCRP-1	1	Sample dotted with grease
-2	1	Silicon metal on surface
-3	1	Short cycle only
-8	1	Short cycle only
-9	1	Sample marked with Al pen
-10	4	Sample wiped with grease
-13	4	
-16	4	
-17	4	
-21	4	Sample marked with Al pen
-22	3	SiC grain
-23	3	Surface masked
-24	5	Poor preparation
-25	6	
-26	5	Sample dotted with grease
-28	2	
-29	2	
-32	2	
-33	6	
-35	2	
-38	2	
-39	3	Silicon metal
-40	3	Added release agent
-41		
-42	5	Heavy release agent one side
-43	3	Sample close to retort wall
-44	5	Silicon metal spot
-45	6	Sample dotted with grease
-47	6	SiC sprinkled
-48	5	

Run No. 1 - Goal to produce thin (<0.009 in.) coating
Run No. 2 - Goal to produce 0.014 to 0.017 in. coating
Run No. 3 - Goal to produce 0.018 to 0.023 in. coating
Run No. 4 - Goal to produce defect samples with 0.014 to 0.020 in.
Run No. 5 - Goal to produce coatings with variable thickness
Run No. 6 - Goal to produce 0.010 to 0.015 in. coating

Table 6. Coating Process Information for ACCRP Specimens.

Specimen	Coating Run	Defects/Sample Preparation (Normal Unless Noted)
K650-65	4	Grease, poor sample preparation
-66	4	Poor preparation, SiC metal
-67	4	No surface preparation
-70	4	Marked with Al pen
-71	1	Sample dotted with grease
-73	1	Silicon metal spots
-74	1	Short cycle only
-75	1	Short cycle only
-76	1	Al pencil mark
-77	3	SiC grain
-79	3	Release agent
-80	3	Silicon metal
-81	3	Heavy release agent
-82	3	Sample next to wall
-83	6	Poor preparation, release agent
-84	5	Poor preparation
-85	5	Sample dotted with grease
-86	5	Release agent varied
-88	5	Silicon metal
-89	6	
-90	5	
-92	2	
-93	2	
-97	6	
-99	2	
-102	2	
-107	2	
-110	6	
-111	6	Poor preparation

Run No. 1 - Goal to produce thin (<0.009 in.) coating
Run No. 2 - Goal to produce 0.014 to 0.017 in. coating
Run No. 3 - Goal to produce 0.018 to 0.023 in. coating
Run No. 4 - Goal to produce defect samples with 0.014 to 0.020 in.
Run No. 5 - Goal to produce coatings with variable thickness
Run No. 6 - Goal to produce 0.010 to 0.015 in. coating

Table 7. Coating Thickness for ACCRP Specimens.

Technique/	Dimensional Measure		Eddy Current			Metal-lography	Computed Tomography	
Specimen	SoRI	GE	LTV	GE		SoRI	SoRI	GE
ACCRP-1	2.2	2.5	5-7	4	5		471	450
-2	2.4	3.0	4-5	5	3		492	425
-3	4.0	4.5	4-6	3	5		459	
-9	7.5	7.5	4-6	4	3		444	441
-10	5.4	2.5	14-20	13	17	17.3 19.4	628	522
-13	8.7	3.5	17-23	13	17	16.5 20.5	512	564
-16	4.2	4.0	14-18	12	18		557	600
-17	10.9	9.5	14-16	17	16		535	577
-21	12.8	11.0	14-15	16	16			
-22	7.8	6.0	22-24	18	20		710	647
-23	12.3	2.5	19-22	27	25		804	669
-24	3.3	3.5	16-18	14	15	21.7 19.3	614	634
-26	3.4	3.5	14-19	15	16	19.5 22.3	712	682
-28	3.0	2.5	11-16	12	17		544	613
-29	3.5	4.0	13-15	13	13		568	544
-32	3.1	3.5	13-15	12	13	14.5 18.0	567	569
-35	3.5	3.0	14-15	12	15	15.0 14.3	561	650
-38	3.2	3.0	13-16	13	15	13.0 15.5	567	637
-39	5.9	7.0	19-39	20	19	22.2 22.5	722	770
-40	6.2	5.6	18-23	17	21		692	722
-42	4.7	5.0	17-20	19	18		578	641
-43	4.7	5.0	17-23	17	20	23.5 22.2	636	624
-44	8.7	7.5	10-18	14	16		480	325
-45	3.8	4.0	12-14	14	19		652	659
-47	5.0	6.3	N/A	16	18	16.0 21.6	577	574
-48	3.4	3.0	15-21	15	18	19.0 19.2	599	637

Notes: 1. All measurements shown are in mils except Computed Tomography, which are shown in maximum raw count form (Hounsfield scale).
2. Eddy Current measurements based on lift-off technique correlation.
3. Computed Tomography data was taken by Southern Research and reduced by General Electric.

Table 8. Coating Thickness for K650 Specimens.

Technique>> Specimen	Dimensional Measure		Eddy Current			Metallography		Computed Tomography	
	SoRI	GE	LTV	GE		SoRI		SoRI/GE	
K650-65	1.8	2.5	14-15	12	11			511	526
-66	1.8	5.0	14-16	14	8			551	543
-67	1.8	2.0	14-16	11	10			524	513
-69	1.1	1.5	N/A	10	12			525	538
-70	2.0	2.5	14-15	12	11			520	511
-71	1.4	1.5	5-7	3	2			404	377
-74	0.8	1.0	5-7	2	2	5.7	6.2	387	399
-75	1.1	1.0	5-7	2	3	7.2	9.5	326	424
-76	1.3	1.0	5-7	2	2	5.2	4.4	333	416
-77	1.8	2.0	18-22	11	16			550	617
-79	2.8	9.5	17-24	4	7				
-80	2.0	2.0	18-21	15	14	16.1	14.1	572	547
-81	1.8	2.5	17-20	12	11	17.9	16.3	571	545
-82	1.8	3.5	17-20	12	9			551	517
-83	2.0	2.5	9-10	10	10			584	576
-84	2.1	2.5	10-11	12	12			482	546
-85	1.4	1.5	10-12	10	10	13.5	16.6	572	555
-86	2.3	2.5	11-16	12	9			540	502
-88	4.6	10.0	10-16	19	N/A				
-90	1.6	1.5	10-11	10	10	13.3	15.3	526	585
-92	1.5	1.5	13-15	10	9			457	517
-93	1.5	1.5	13-15	9	9			525	485
-99	2.0	1.5	13-15	10	8			472	515
-102	1.4	1.0	13-15	10	9			511	463
-107	1.1	1.5	14-17	9	8			515	471
-111	2.0	1.5	7-10	11	10	12.7	11.4	538	529

Notes: 1. All measurements shown are in mils except Computed Tomography which
         are shown in maximum raw count form (Hounsfield scale).
         2. Eddy Current measurements based on lift-off technique correlations.
         3. Computed Tomography data was taken by Southern Research and reduced
         by General Electric.

3.4 COATED TEST COUPONS

Measurements were made on the coated test coupons using CT radiography, film radiography, beta backscatter, eddy current, and infrared methods. These methods were used to generate the correlations to coating thickness discussed Section 10. The physical dimensions, weights, and calculated densities of the coated coupons are given in Tables 1 and 2. In addition, thermal expansion tests were performed.

3.4.1 CT Radiography

CT radiography was performed on all coated coupons using a GE CT9800 scanner at Baptist Montclair Hospital, Birmingham Alabama. In order to reduce the artifacts observed in previous scans (see Section 3.2), the stacking arrangement was altered. A cylindrical holding fixture was made which held up to 14 coupons in a circular arrangement with coupons not aligned or parallel to each other to reduce edge artifacts. Two coupons and one cylinder of graphite were also included as density references. The cylinder was packed with flour around the coupons to act as a bolus and further reduce artifacts. Details from the scans are compared with post-oxidation CT images in Figure 7.

An investigation was made of the usefulness of CT radiography to measure coating thickness. A direct measure of thickness cannot be made from the CT image because the image does not have sufficient resolution. The resolution of the CT9800 is approximately 0.02 inch, and coating thickness requires measurements over the range of 0.005 to 0.030 inch with an accuracy of a few thousandths of an inch. However, the CT image does change as a result of varying coating thickness, and this can be used to estimate the thickness. As a very simple analysis, the peak CT number was extracted as shown in Figure 8a and was plotted against coating thickness determined by metallography. The plot is shown in Figure 8b. A more sophisticated approach would be to model the expected CT profile across the coating, as described in Reference 2.

3.4.2 Film Radiography

Conventional film radiographs of coated coupons are shown in Figure 4. The edge radiograph (X-ray beam parallel to specimen width) shows delamination in Specimen 24. The dark contrast of this feature after coating indicates that some coating has occurred on the surfaces of the delamination.

3.4.3 Beta Backscatter

A series of measurements were made on the coated coupons using a beta backscatter technique. The primary purpose was to assess the effectiveness of the technique for measurement of coating thickness. Equipment used was the Betascope 2000 manufactured by Twin Cities Testing. This instrument permits a choice of various isotope sources according to the electron energy required. The operating principle of the instrument is based on the change in electron
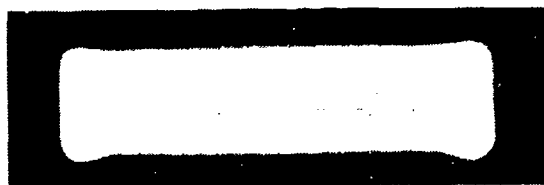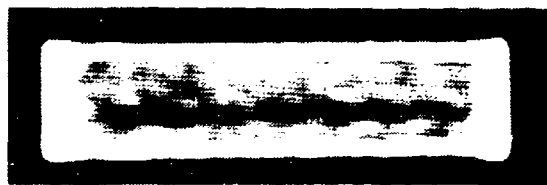
23
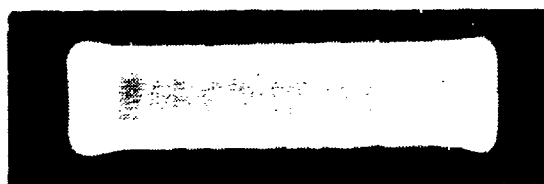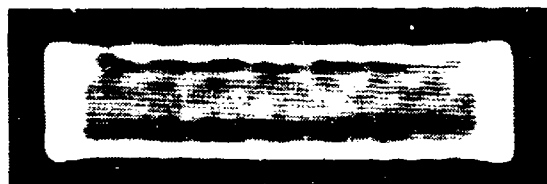
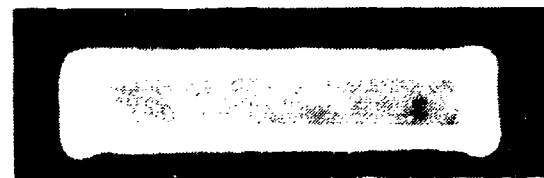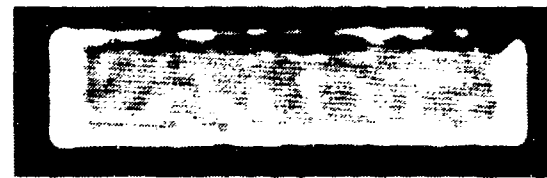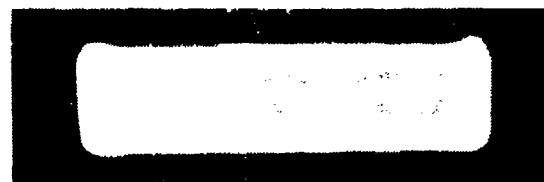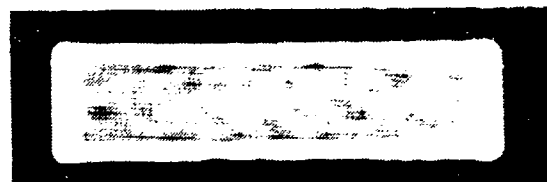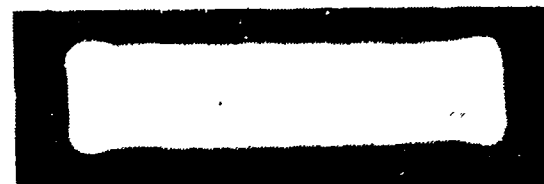|		
a	28	b
c	29	d
e	70	f
g	77	h
i	82	j
k	93	l
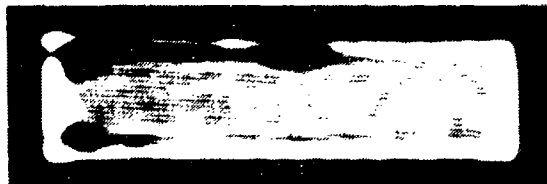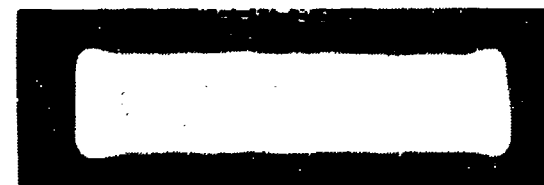
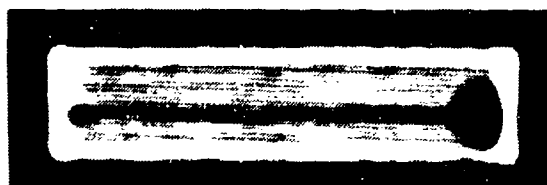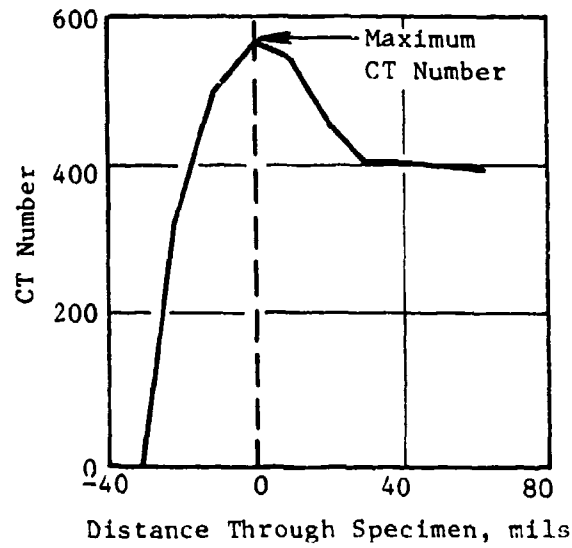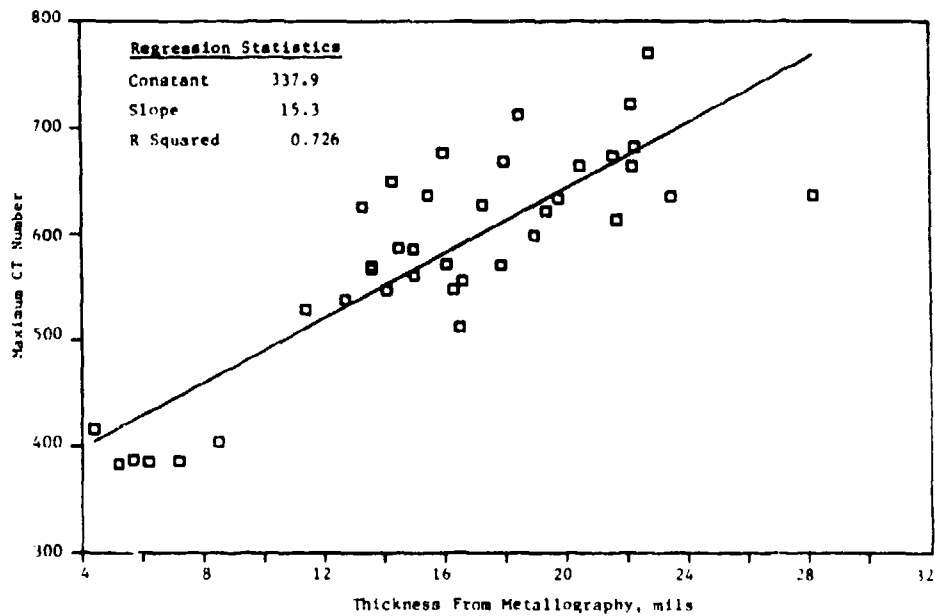Before Oxidation Test · · · · · · · · · · · After Oxidation Test

Figure 7. X-ray CT Scans of Coated Coupons Before and After Oxidation Testing.

(a) Derivation of Maximum CT Number

(b) Correlation of Maximum CT Number With Metallographically
Measured Thickness

Figure 8. Estimates of Coating Thickness From X-ray CT Image.

25

scattering and absorption cross sections as a function of atomic number and density. A dense material will backscatter more electrons than a less dense material. If there is a difference in scattering properties between substrate and coating, then the total backscatter will be a function of the coating thickness, provided the electron energy is high enough to penetrate into the substrate but low enough for significant scattering. Three isotope sources were initially evaluated:

Promethium 147	0.22 MeV
Strontium 90	2.18 MeV
Rhodium 106	3.53 MeV

Initial evaluation of the sources showed that the 0.22-MeV electrons from the promethium source were unable to penetrate the coating, and backscatter count rates from the rhodium isotope were very low (approximately 16 per second), indicating very little backscatter. The strontium isotope gave more useful count rates that varied with expected coating thickness, so this source was used for further measurements.

Backscatter measurements were then made on all coated coupons using the strontium 90 source. Six readings were taken on each coupon, three on each face, at distances 0.5, 1.5, and 2.5 inches from the end of the specimen, and along the lateral centerline. Counting was for 100 seconds for each measurement, and the results were tabulated as counts per second (Tables 7 and 8). In addition, the same measurement was made on samples of uncoated material (K650 and ACCRP) and on dense, sintered, silicon carbide. The purpose of these measurements was to correlate the results with coating thickness to be measured metallographically; this correlation, shown in Figure 9, is discussed in Section 10.4 of the report.

3.4.4 Eddy Current Measurements

Eddy current thickness measurements were made at the same six locations on each coupon. Initially, a thickness calibration curve was produced using pieces of uncoated K650 and ACCRP materials and pieces of plastic shim stock of known thickness to simulate the coating. The eddy current reading depended on shim thickness in an exponential decay (as expected), allowing an empirical equation to be used for thickness up to 0.025 inch:

$$\text{Thickness} = 0.093 \log (X_0 - X_{inf})/(X_c - X_{inf})$$

Where X_0 and X_c are eddy current readings on substrate standard and coating surface, respectively, and X_{inf} is the reading with the coil far from the substrate.

Coating thicknesses were then estimated from this equation, and Figure 10 correlates the results with thickness measured metallographically. Figure 11
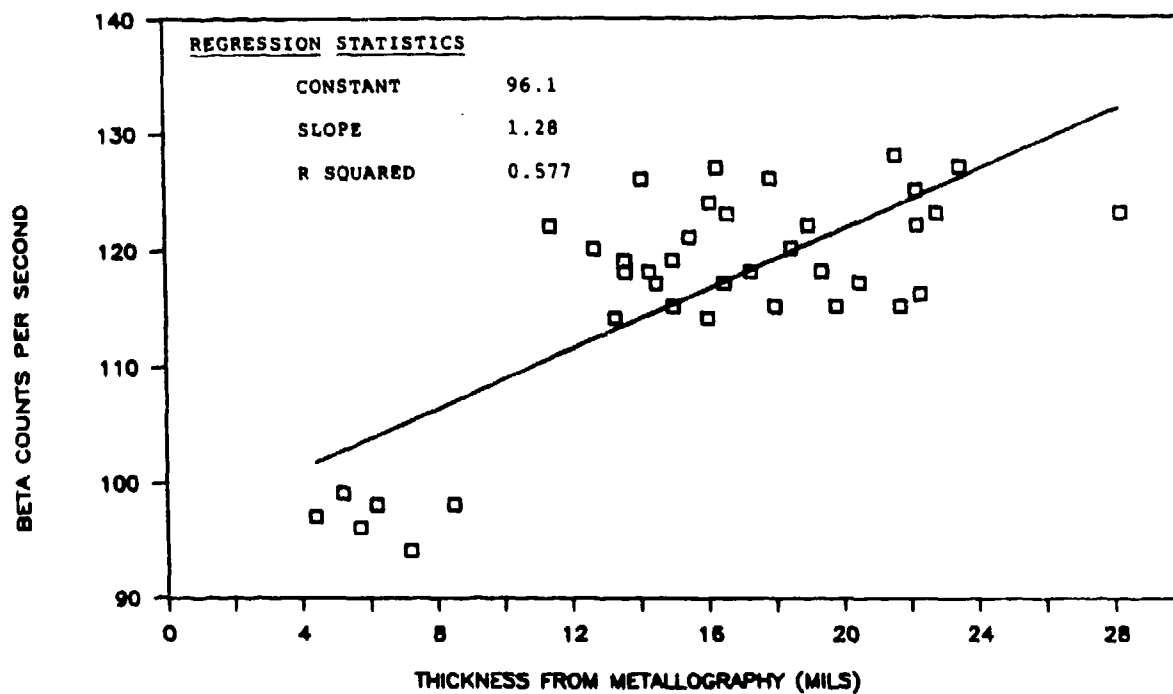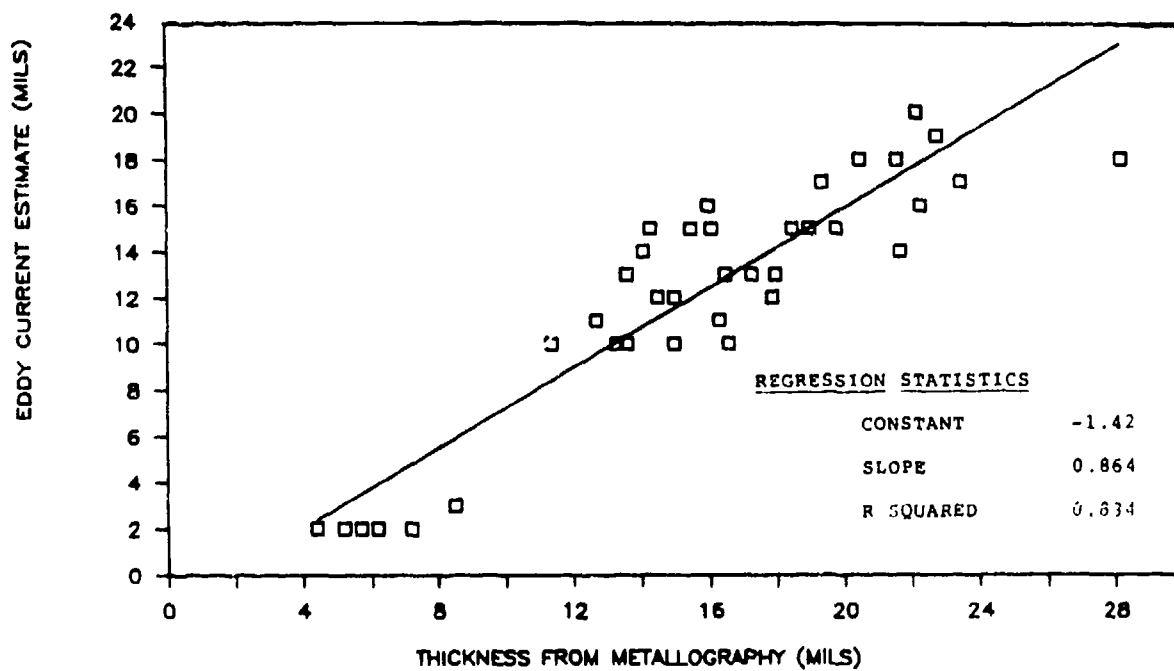
Figure 9.   Beta Backscatter Results

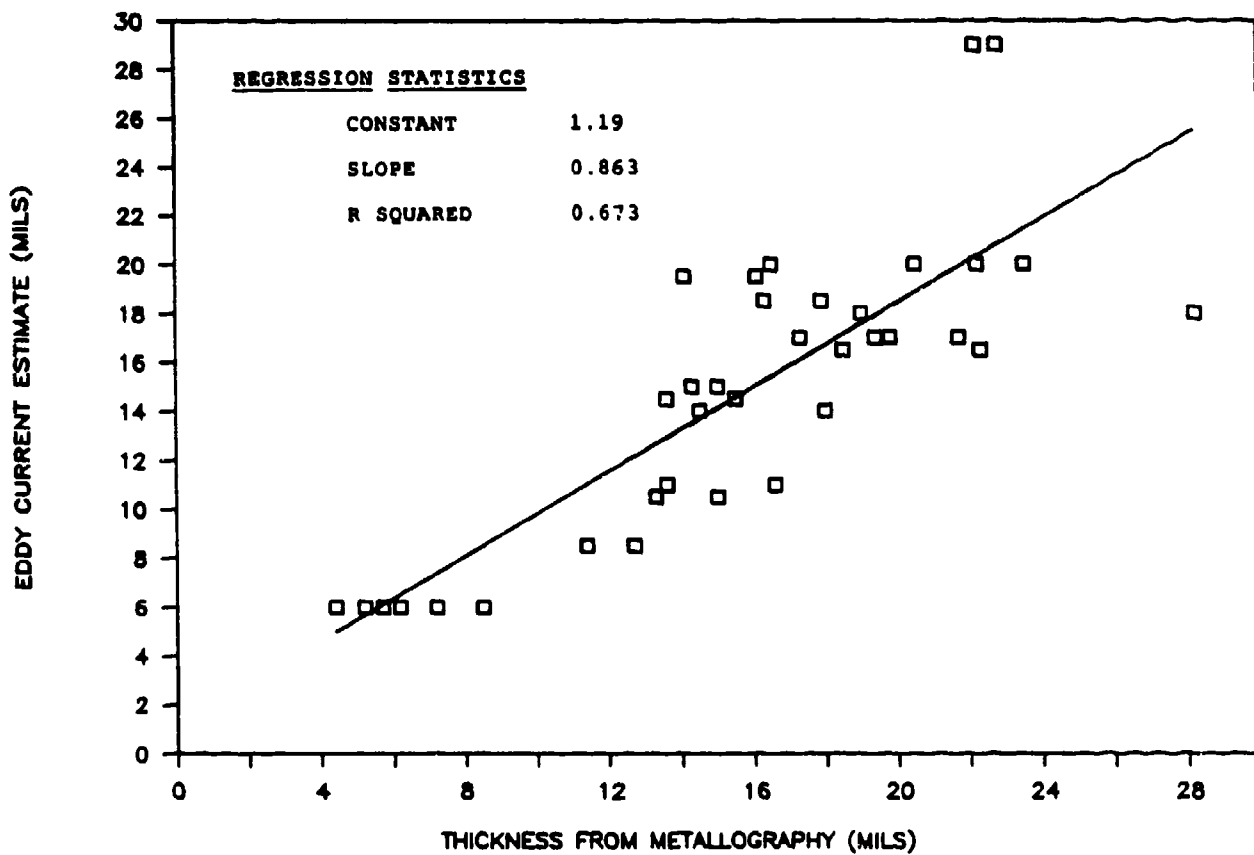Figure 10.   Eddy Current Coating Measurements (GE Data).

27

Figure 11. Eddy Current Coating Measurements (LTV Data).

is a plot of the eddy current estimates of thickness supplied by LTV. The correlation between eddy current measurements and coating thickness and the significance of the results will be discussed in Section 10.2 of the report.

3.4.5 Thermal Expansion

Thermal expansion was measured on six coated coupons, three for each plate representing the warp, fill, and 45° off-axis directions. The coated specimen ends were removed to prevent adherence and false disturbance to the test apparatus. The warp-aligned specimens were also tested at an intermediate test temperature (2400° F) to analyze the effect of thermal cycling on the test coupons. Samples for scanning electron microscope (SEM) analysis were extracted from the thermal-expansion specimen ends after each test run; Figures 12, 13, and 14 show the results.

As expected, free thermal responses were not identical for warp, fill, and 45° off-axis coupons of either material. This was due to the differences in elastic stiffnesses in the various directions. The internal strain levels induced by the mismatch of thermal expansion coefficients for coating and substrate materials (seen in Figure 6) are determined by the shared loading of the two materials and by the respective stiffnesses. Thus, the off-axis coupons, being softer in that direction, accepted greater internal strain levels, and this translated into the higher thermal expansion observed. The warp and fill directions have similar stiffnesses (the fill direction being slightly less stiff), and so the expansions were likewise similar. The K650 material had higher thermal expansions in the warp and fill directions, a reflection of higher uncoated in-plane expansion and lower uncoated stiffness. The 45° off-axis expansions of the two materials were nearly identical.

Typical cyclic data are shown in Figure 14. Note that the initial test run, done by quartz dilatometry, was higher than the succeeding runs done by graphite dilatometry. This may be due to the presence of a sealant layer. Above the softening temperature of the sealant, typically around 1200° F, the tensile stresses induced in the substrate are somewhat relaxed, and the net expansion (as measured on the substrate centerline) decreases. Additional damage of the sealant layer and the underlying conversion layer has been observed in prior studies. The sealant layer applied after a pack cementation process, as reported by LTV, was not readily apparent in SEM evaluations but was isolated using polarized-light metallography. The graphite runs performed to 2400° and 2800° F, respectively, yielded essentially identical expansion responses. The minor differences witnessed at low temperatures were probably due to the limited accuracy of temperature measurements in the graphite facility in that range.
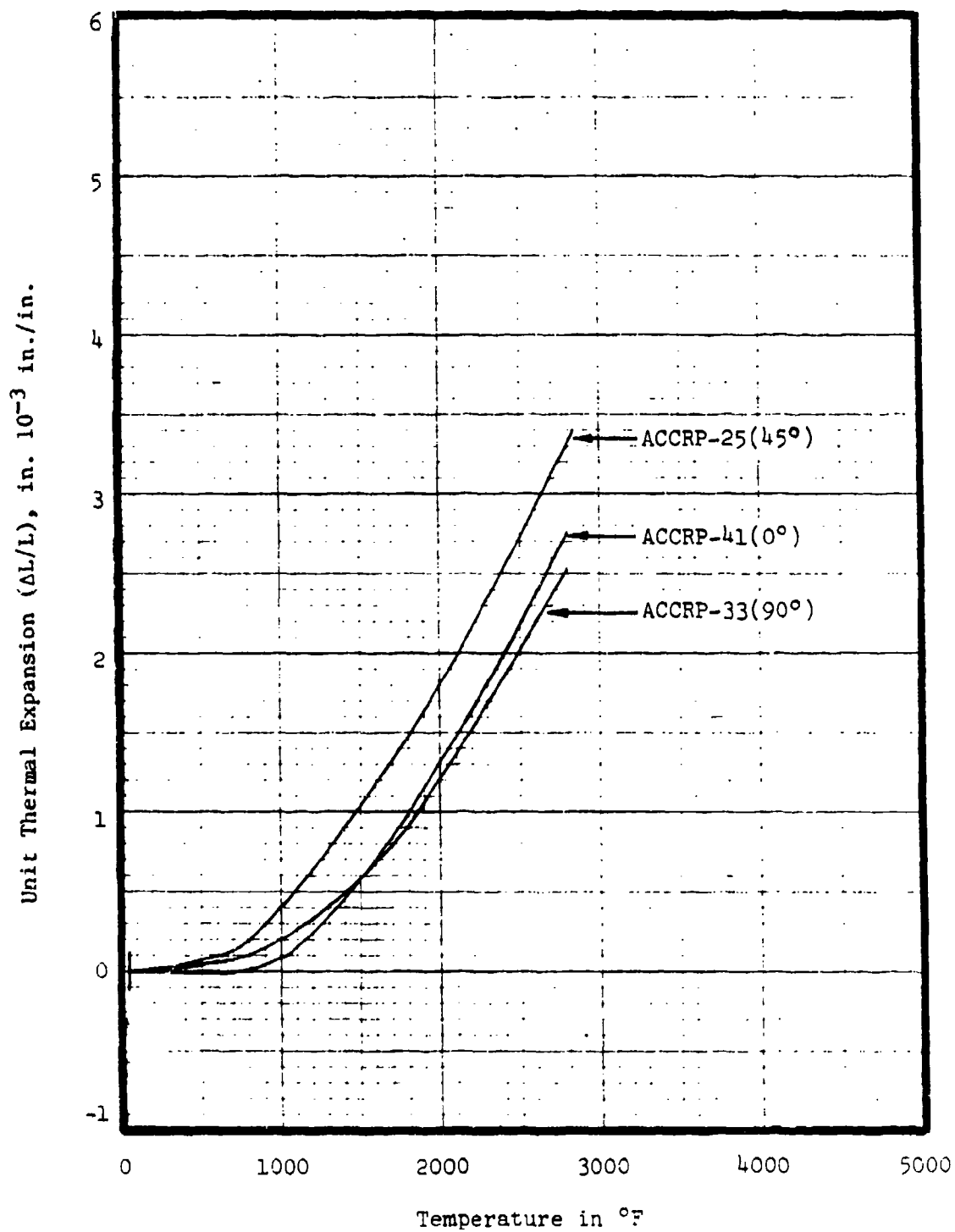
29

Figure 12. Thermal Expansion Results for the Coated ACCRP Materials.
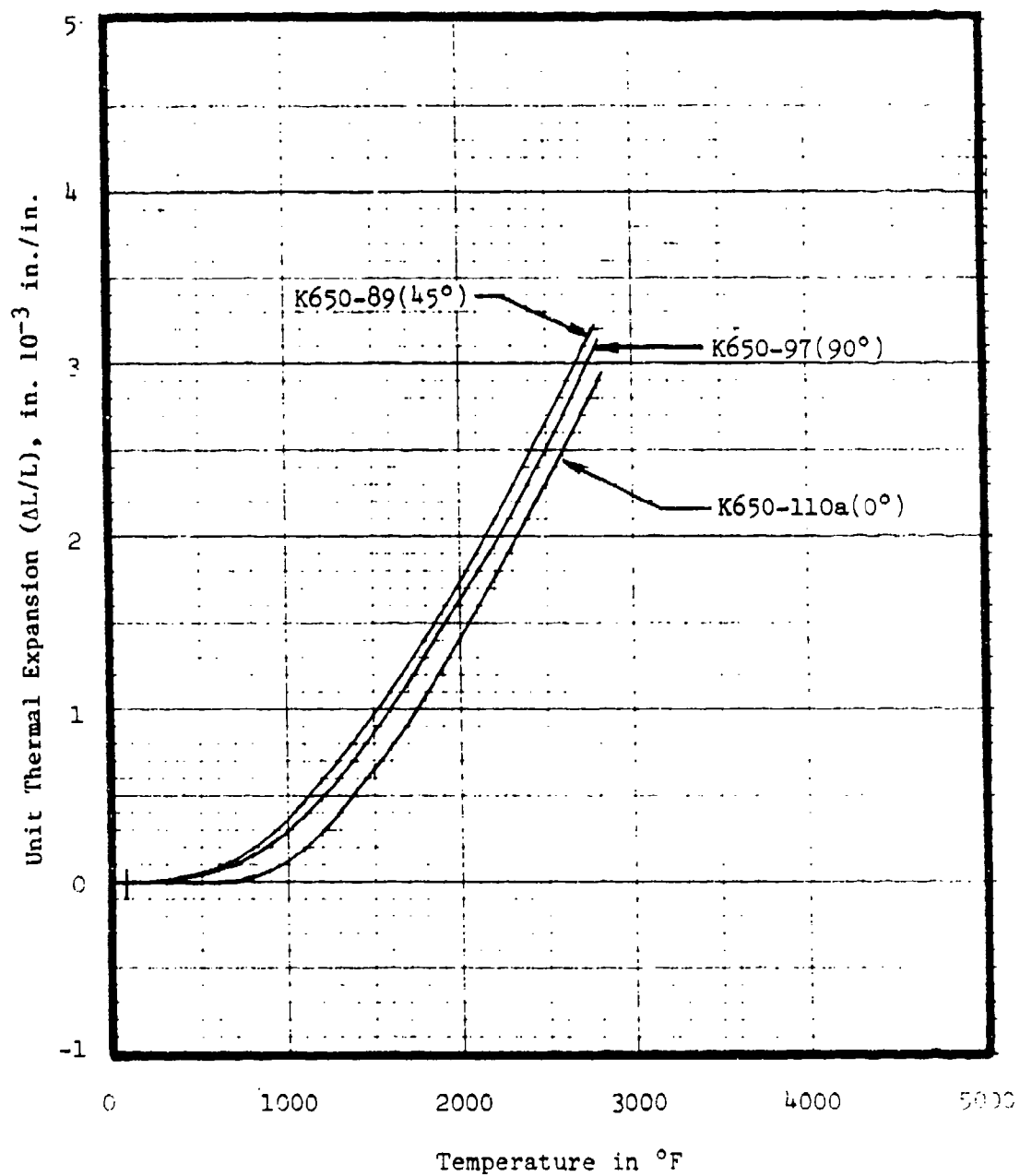
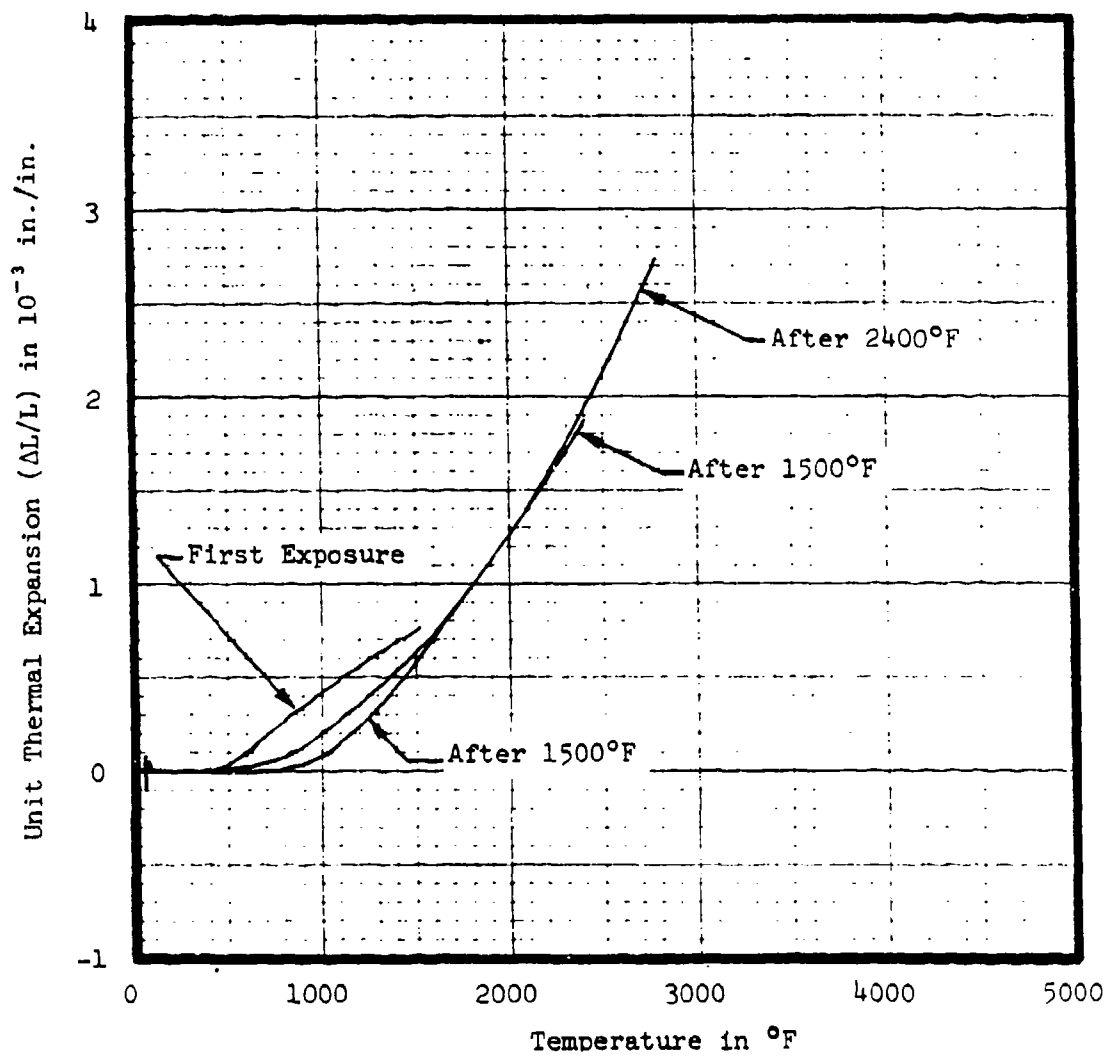Figure 13. Thermal Expansion Results for the Coated K650 Materials.

Figure 14. Effects of Thermal History on the Thermal Expansion of Coated 2D C-C Material.

4.0 DEVELOPMENT OF DIFFERENTIAL-ABSORPTION TECHNIQUE

The differential-absorption technique is an adaptation of the liquid or dye penetrant method. It utilizes the differences in absorption rate between the coating and the substrate to preferentially deposit fluorescent particles. The fluorescent particles tend to gather near cracks, or other such defects, in the coating layer which provide an absorption path to the underlying substrate. Thus cracks that do not penetrate the entire coating thickness should not appear as intense as those that do. This corresponds with the program objective to be able to identify cracks selectively which provide paths for oxidation.

4.1 COATING CHARACTERISTICS

An important part of the optimization of a technique is characterization of the environment in which it is used. For differential absorption, the environment consists of the coating layer itself and the cracks in which the flourescent particles seat themselves. The majority of this investigation was performed using an ETEC Autoscan SEM. Additional insight was gained during the performance of metallography at the end of the program.

Crack size and depth were measured initially by SEM. The average crack width was found to be approximately 10 μm with a range of 5 to 15 μm. The typical crack extended completely through the coating layer; in the inner few mils the cracks were submicron in width (visible only at high magnification). Later, during inspection of oxidized coupons, submicron width cracks were discovered on the surface. These rarely penetrated the coating layer. Figure 15 shows the profile of typical cracks witnessed in the coated coupons. Also in the figure some interlaminar cracks are noted. These propagated from the tips of the cracks extending through the coating layer along or just underneath the coating-to-substrate boundary. These were probably generated by shear-lap stresses upon cool-down. Additional transverse cracking was noted within the coating layer itself along cristobalite deposits.

The coating layer consisted of a surface sealant layer and a substrate conversion layer. The conversion layer was formed by pack cementation, and metallography indicated very little coating porosity in this region. The sealant layer resided almost entirely on the surface and had a void content approaching 80%. The dimensional differences between uncoated and coated coupons (see Tables 1 and 2) were essentially the thickness of the sealant layer.

The surface texture of the coated coupons prior to oxidation was fairly rough; this caused some microcapsules to become trapped in the surface away from the cracks. The result was areas of high background intensity, often obscuring crack indications. After oxidation the surface became glass-like, and background intensity was less a problem. Figure 16 shows the progression of surface texture as surface oxidation progresses. Figure 16c shows the bottom surface of a typical oxidized specimen. The surface was situated over
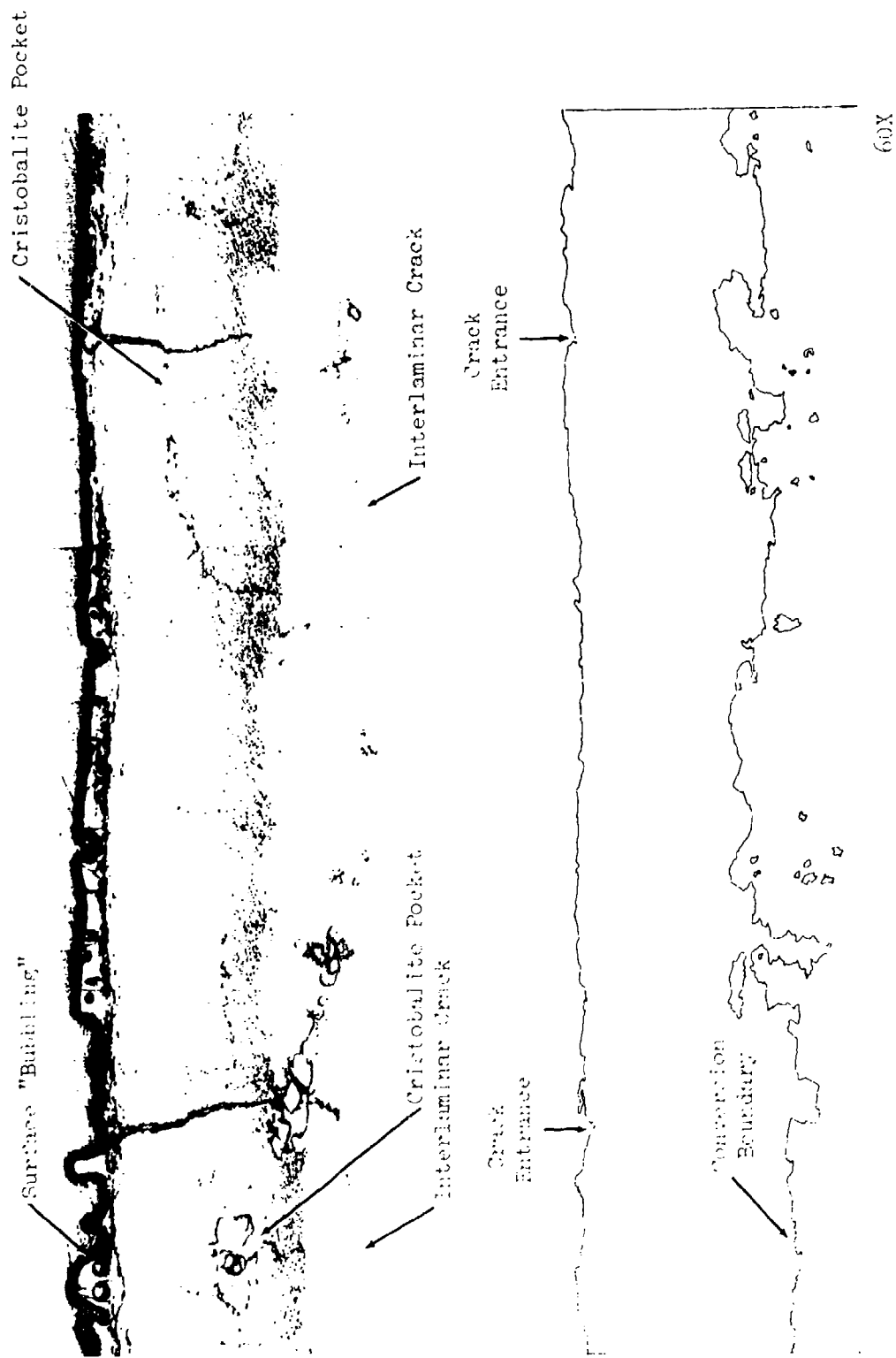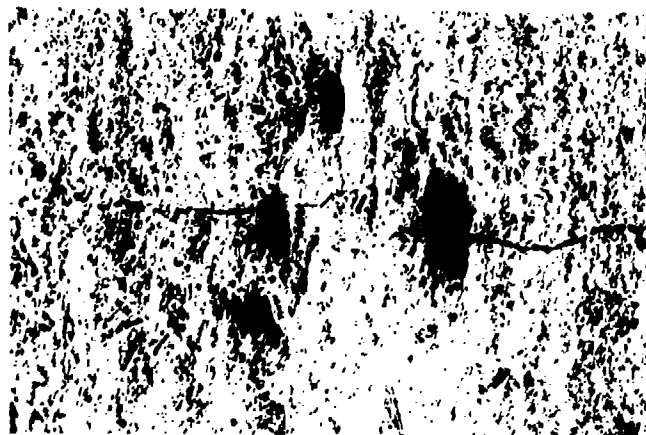
Figure 15. Metallographic Indications Seen in Typical Coated 2D C-C Coupon (Specimen Shown).

(a) As-Received Condition
(Dark Areas Represent
Surface-Charging)

(b) After Exposure to 2450° F
in Air – Top Surface

(C) After Exposure to 2450° F
in Air – Bottom Surface

Figure 16. Surface Alterations due to Thermal Exposure in an Oxidizing Environment (Hour Heat Soak).

35

fire-brick and thus experienced lower oxygen flow. This is discussed further in Section 5.2.

As mentioned above, cristobalite formations were noted within the coating layer. Figure 17 shows a typical "pocket" of cristobalite with characteristic crystalline structure. X-ray diffraction scans were performed on powdered samples of coating material. Figure 17 shows the results obtained for as-received samples and those which had been heat soaked at 2450° F in air for one hour. The change in the relative peak heights was believed to be due to random scatter in the samples rather than the additional formation of cristobalite. This was supported by later diffraction scans of material after extended heat soak.

4.2 DYES AND ENCAPSULATION

During the course of the program, polymer microspheres containing various core materials were prepared. Table 9 lists all of the preparations. The

Table 9. Microcapsule Preparation used for Differential Absorption Techniques Optimization.

Microcapsule Batch 099o	Color (1)	Core Material	Theoretical Core Loading Wt %	Particle Size Range um	Comments
-004-1	Blaze Orange	None	--	1-5	
-00o-1	Blaze Orange	None	--	0.5-3	
-014-2	Aurora Pink	Barium (2)	(3)	3.5-3	
-025-1	Saturn Yellow	None	--	0.5-10	Fibrous microparticles
-041-2	Saturn Yellow	None	--	0.3-1	
-045-1	Rocket Red	None	--	3.4-3	
-049-1	Rocket Red	None	--	1-5	
-056-1	None	Boron	50	3.15-1	Dark-colored from core material.
-051-1	Horizon Blue	Boron Carbide	50	0.15-1	Dark-colored from core material.
-074-1	Blaze Orange	None	--	0.5-3	
-090-1	Blaze Orange	None	--	5-15	
-095-1	Blaze Orange	Milled Glass (4)	50	2.5-3	Glass Batch 099o-242-2
-099-1	Blaze Orange	Milled Glass (5)	50	0.2-10	Glass Batch 099o-24-4

Notes:
1. Tradenames of the Dayglo Color Corporation, Cleveland, Ohio.
2. The Barium is held to the surface of the microspheres by ionic bonds.
3. Core loading was not determined.
4. This glass was reported to contain amounts of Cesium Oxide.
5. This glass was reported to contain amounts of Titanium Carbide.

36

(a) Cristobalite Formation in the Coating Layer
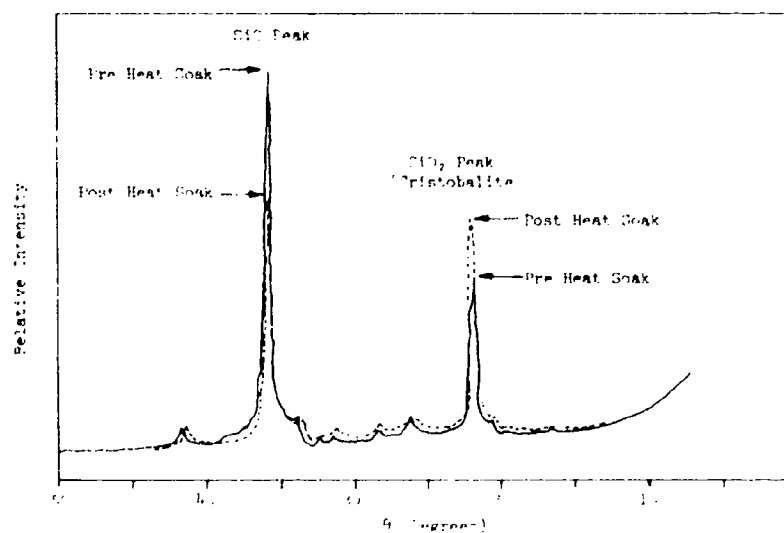
(b) X-ray Diffraction Results for Pre- and
Post-Heat Soak of Coating Material

Figure 17. Indications of Cristobalite
Structure in Coated Coupons.

37

microspheres of polymer were uniformly colored and had smooth surfaces. In general, the microcapsules were spherical and monolithic (the core material was dispersed with the polymer matrix rather than externally attached). In the microencapsulation process, the core material was dissolved or dispersed in an organic solution of the polymer material, and the resulting mixture was processed to provide finished microcapsules. The resulting microcapsules were washed free of processing aids by centrifugation and then freeze-dried.

The polymer material used for almost all of the microcapsule batches was Type 685D polystyrene (Dow Chemicals). Core materials used were flourescent dyes extracted from Dayglo flourescent pigments (Dayglo Color Corp.), barium, boron, boron carbide, and two milled borate glasses. The polymer matrix used by Dayglo for flourescent pigments is not soluble in most solvents, but the dyes are soluble in many organic solvents; consequently, the insoluble polymer was extracted in a preliminary step, and only the flourescent dye was used. The theoretical core loading of the microcapsules containing glass formers or metal ions was 50%. Core loadings for dyed microcapsules were not calculated. The copolymer of one batch of microcapsules was made from maleic anhydride. In subsequent steps, the anhydride units were hydrolyzed to carboxylic acid units to which barium tracer ions were attached. This batch was made in an unsuccessful attempt to visualize crack patterns with the electron diffraction scanning capability of the ETEC Autoscan unit.

Microencapsulated particles were used in this project primarily because size distribution could be controlled in processing. Existing dye penetrant solutions often contain particles with a broad range of sizes and asymmetrical configurations. On coated coupons, use of these solutions often produced images almost obscured by background intensity caused by entrapment of the very fine particles in the surface roughness. Microcapsulation allowed for optimization and control of particle size. Different batches containing different color dyes representing different size ranges could be produced to isolate cracks of varying widths. Figures 18 and 19 show particle size distributions of the dye and glass-former microcapsule preparations.

Thermogravimetric analyses performed on microcapsule preparations, Figure 20, show there is very little residue after heating to 1100° F. Specimens were cleaned at this temperature between testing of dye preparations.

4.3 CARRIER FLUIDS

The standard carrier fluid used at SoRI was isopropyl alcohol. Table 10 lists the other carrier fluids evaluated and details of environmental impact. Of the other fluids listed, only water exhibited acceptable characteristics as a carrier. The one disadvantage of water as a carrier fluid is the slow evaporation rate. A possible alternative would be to use a mixed solution of isopropyl alcohol and water.

Saturation tests were performed for optimum mix ratios of microcapsules to isopropyl. The results indicated that a mix of 2 grams of microcapsules per liter of alcohol was sufficient.
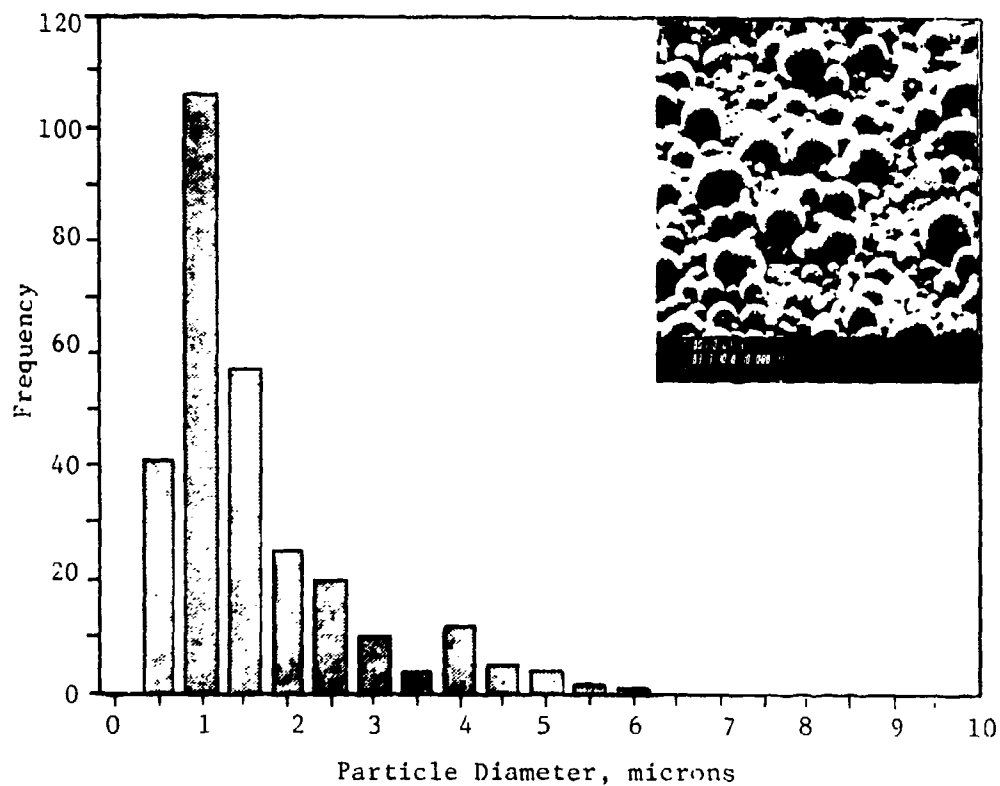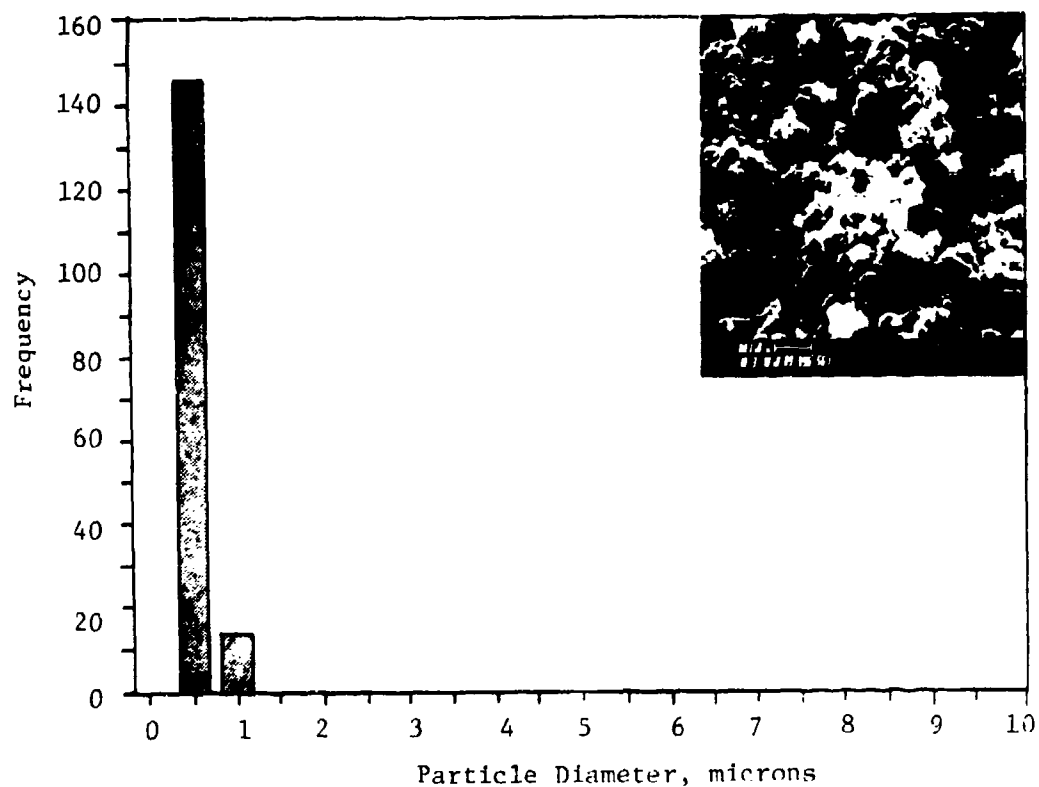
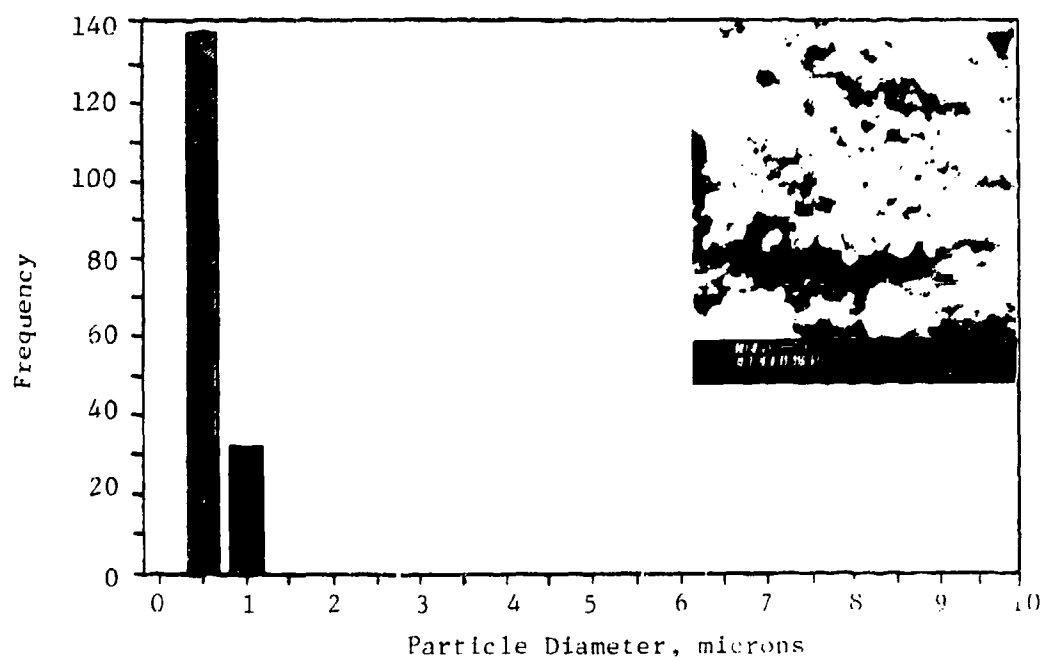(a) Blaze Orange Microcapsules (C996-074-1)
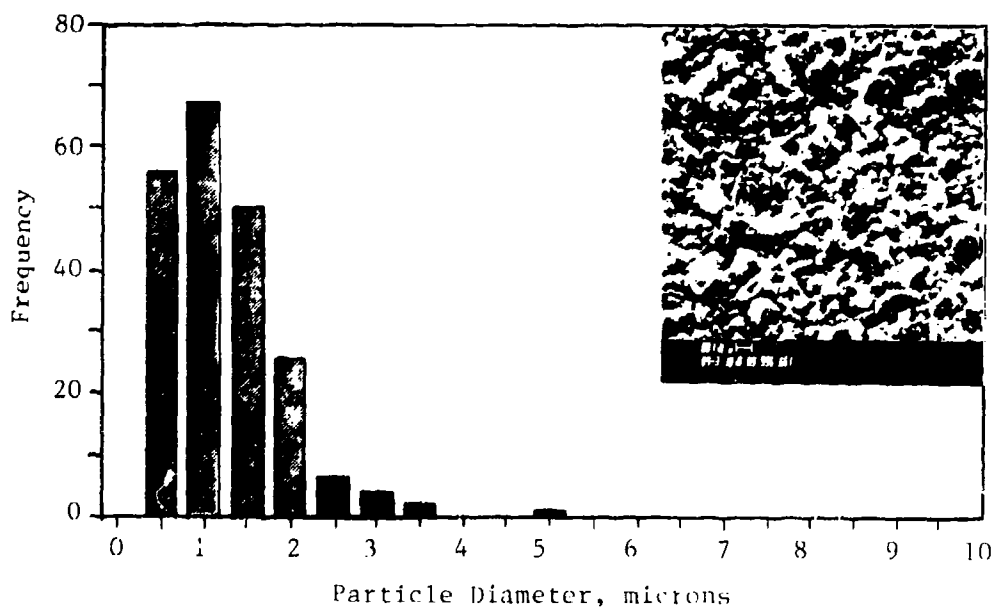
(b) Milled Glass Particles (C996-049-3)

Figure 18.   Particle Size Distribution and SEM Photo of Microcapsule
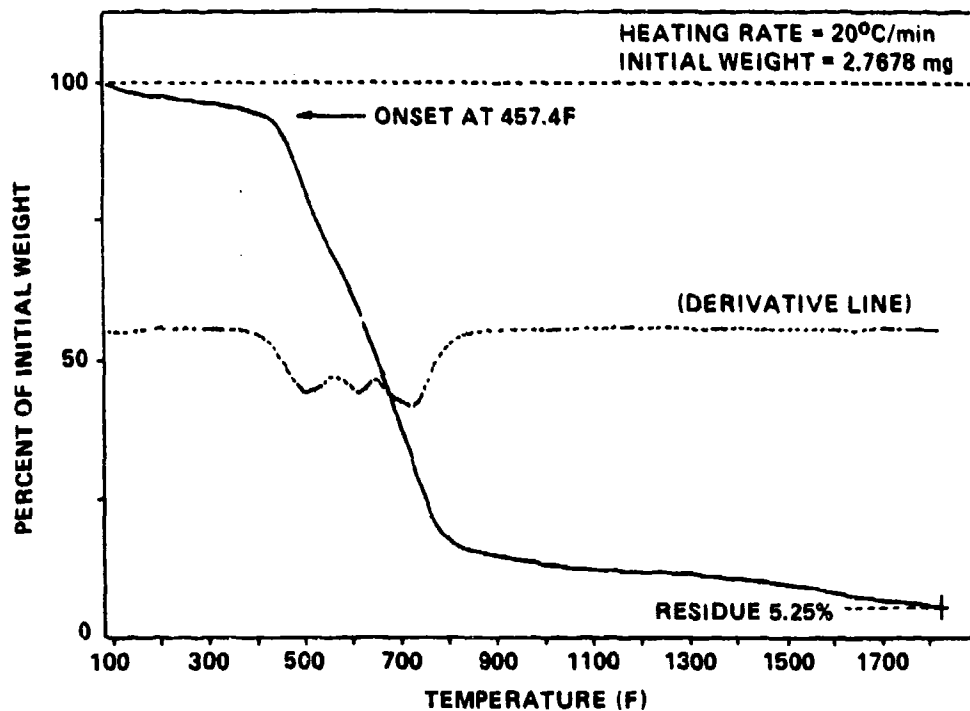Preparations.

(c) Boron Microcapsules (C996-056-1)

(d) Boron Carbide (B_4C) Microcapsules (C996-061-1)

Figure 19.   Particle Size Distribution and Photo of Boron and Boron
Carbide Loaded Microcapsules.

40

HEATING RATE = 20°C/min
INITIAL WEIGHT = 2.7678 mg

ONSET AT 457.4F

(DERIVATIVE LINE)

RESIDUE 5.25%

(a) Decomposition in N_2

HEATING RATE = 20°C/min
INITIAL WEIGHT = 3.5921 mg

PRIMARY ONSET AT 470.2F

(DERIVATIVE LINE)

SECONDARY ONSET
AT 525.8F

RESIDUE 1.79%
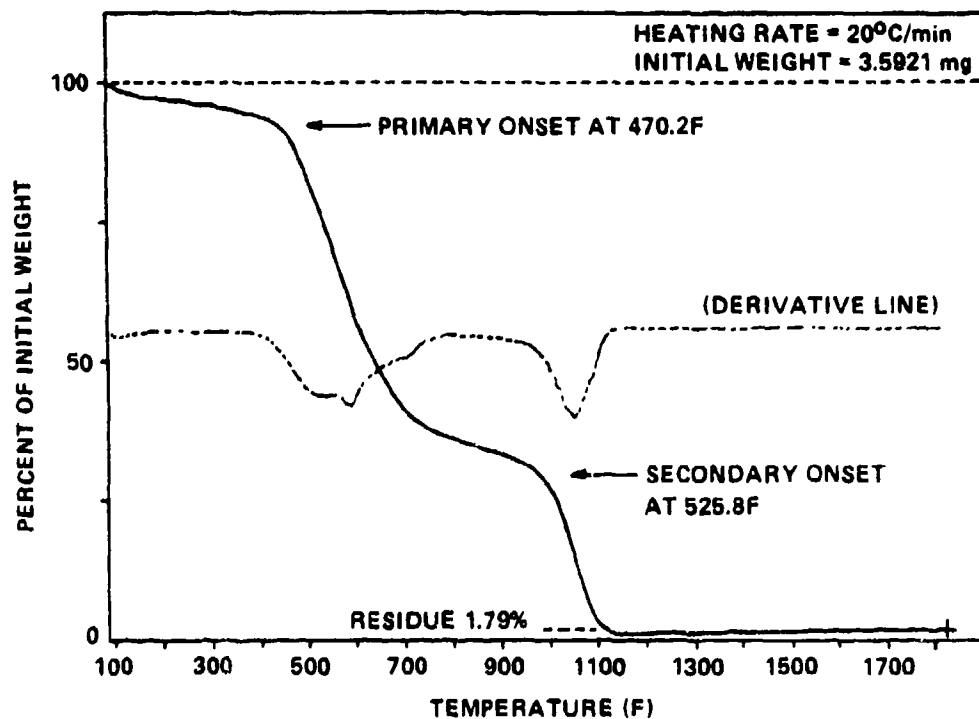
(b) Decomposition in Air

Figure 20.   Thermal Gravimetric Analysis (TGA) of the Thermal
Decomposition of Microcapsules (Batch C996-026-1).

41

Table 10. Survey of Candidate Carrier Fluids for Differential Absorption Technique Optimization.

FLUID / PROPERTY	Water	Isopropyl Alcohol	2,2,4 Trimethyl-pentane	Methanol	Ethanol	Acetone	Mineral Spirits
Chemical Formula							N/A
Alternate Names	--	Iso-propanol	Iso-octane	Wood Alcohol	Ethyl Alcohol	2-propanone	Petroleum Distillate
Specific Gravity	1.000	0.786	0.692	0.791	0.799	0.769	2.752
Vapor Pressure (1)	100.0	82.5	99.2	64.7	78.4	56.5	N/A
Toxicity (2)	--	980	1500	260	1900	2400	1900
Flammable?	No	Yes	Yes	Yes	Yes	Yes	Yes
Soluble in Water?	--	Yes	No	Yes	Yes	Yes	Yes
Solvent for Microcapsules?	No	No	No	Yes	Yes	Yes	Yes
Dispersion	Good	Good	Fair	--	--	--	--
Flocculation (3)	None	Low	Med	--	--	--	--
Leaching	None	None	None	Complete	Partial	Complete	Complete

Notes:

1. The values shown are the temperatures in degrees centigrade at which the vapor of the compound has a pressure of 1 atm.
2. The values shown are the limits for human exposure to air contamination in milligrams per cubic meter of air (US Federal Register Vol.26: No.105)
3. Flocculation is the nonadherent grouping of microcapsules; fluids are rated by the number of microcapsules per group (Low = 5 : 10 = Med = 15).

4.4 FINAL SYSTEM AND APPLICATION

Previous work done at Southern Research using the differential-absorption technique was performed using a two-step procedure. The dye microcapsule suspension was applied with a squirter bottle and then carefully washed (again by squirter bottle application) with clean isopropyl alcohol. This technique was used for the initial documentation of the specimens. Prior to coupon oxidation, the surface roughness mandated the final wash in order to lower the background intensity. After coupon oxidation, poor results were obtained with the two-step approach. The microcapsules were visibly being extracted from the cracks during final wash. Figure 21 shows the loss of indications where a final wash was used. Thus, all documentation of oxidized coupons was taken without the final wash cycle.

Dispersion of the microcapsules was studied to determine the best manner of preparing a microcapsule suspension. The dispersion methods evaluated were hand-shaking, ultrasonic bath agitation, and ultrasonic probe agitation. The results indicated that a 15-minute agitation period using an ultrasonic probe (Fischer Sonic Dismembrator Model 300 or equivalent) is satisfactory.

Considerable effort was expended to ensure that microcapsules were seated properly in the crack microstructure. To this end, microcapsule batches of various size distributions were evaluated. Final tests were standardized using microcapsules with a size range of 0.5 to 3.0 μm in diameter containing Dayglo Orange Dye pigmentation. Figures 22 and 23 show the preferential seating of the microcapsules in and along surface cracks. Investigations indicated that even where there does not initially appear to be total coverage of a crack, the microcapsules can be seen seated within the crack structure (Figure 23 inset).
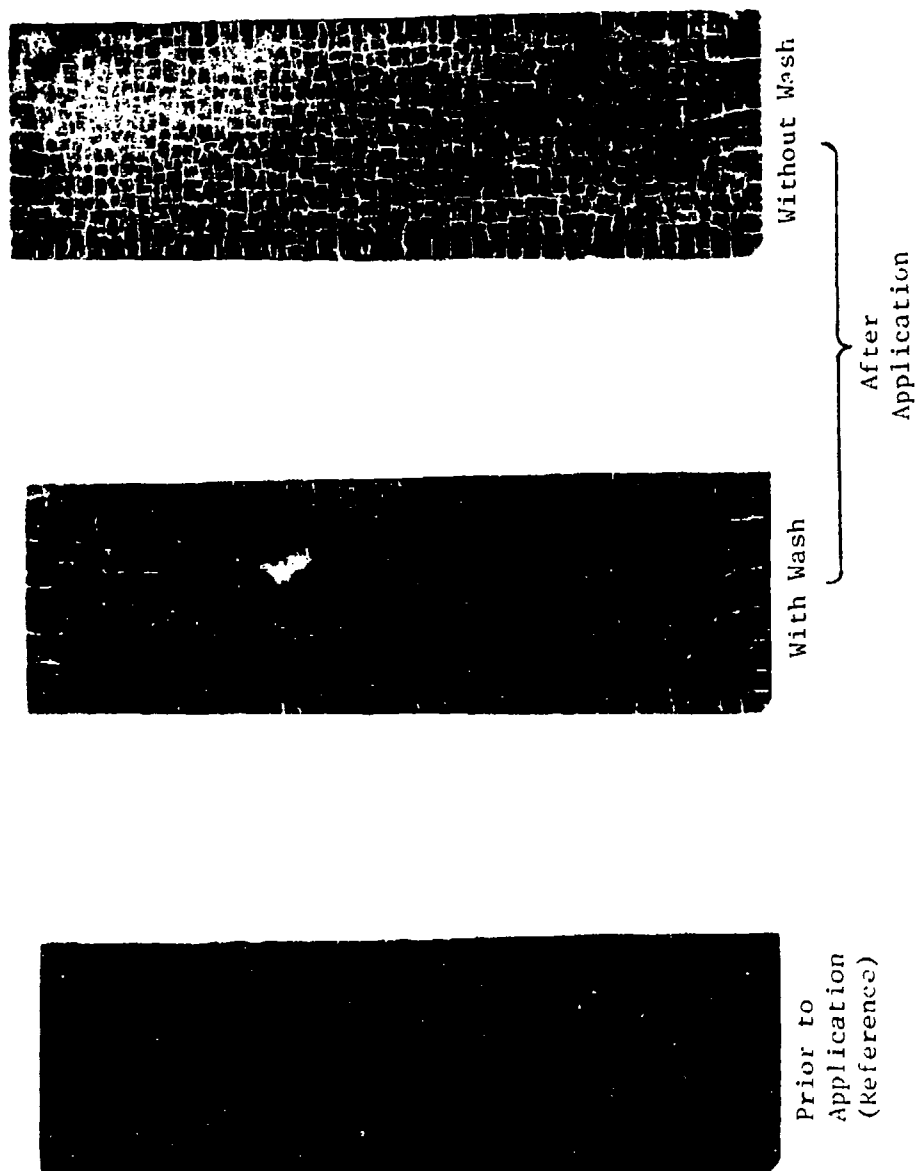
Figure 21. Black-Light Photography of Crazing Pattern in Specimen ACCRP-2 Using Variations in Differential Absorption Technique.
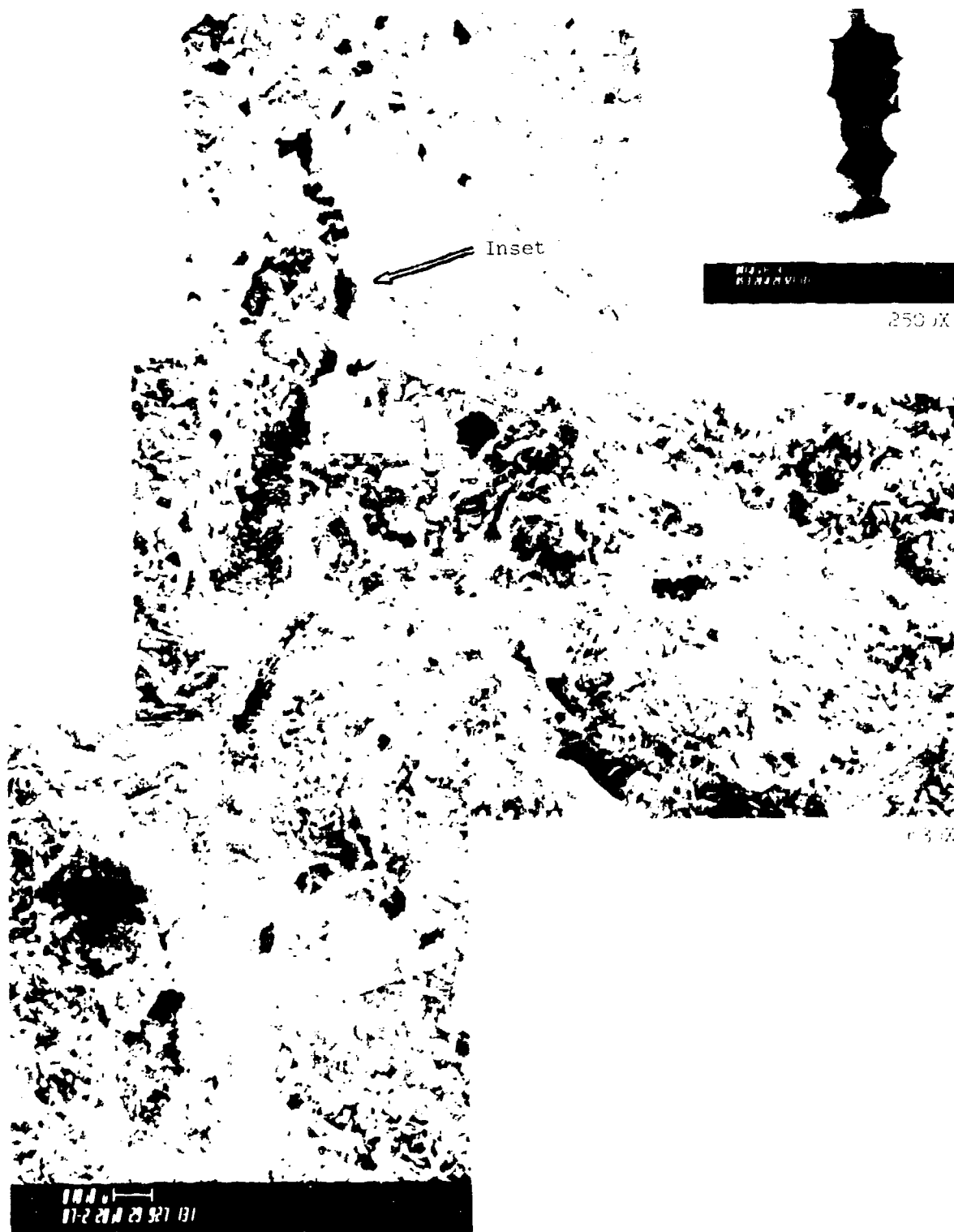
41

Figure 22. Microcapsule Seating in Unoxidized Specimen Taken by SEM.

45

Figure 23. Variations in Microcapsule Seating in Typical Unoxidized Specimen Via SEM Technique.

5.0 METHOD DEMONSTRATION

5.1 HEAT TREATMENT

The test coupons were subjected to a heat treatment comprising one hour at 2500° F in air followed by cooling in air. The purpose of the treatment was to generate stress cracks, as existing cracks were expected to be closed by the final sealant application of the coating process. A small number of coupons showed some signs of oxidation damage and coating delamination at this stage.

The heat treat was also observed to produce a smooth glassy outer layer on the coupons, presumably due to activation of glass formers in the sealant. The formation of the glassy layer was not uniform. Generally, the surface which had been on top during the heat treat exhibited a smooth layer, but the bottom surface, which had been partially in contact with an alumina brick, showed a less smooth surface. This is attributed to slower oxygen replacement on the underside. Coupons treated in a later batch were turned during the heat treatment, resulting in more uniform surface appearance.

A number of coupons showed bubbles in the sealant layer, and in some the glass had apparently stuck to the alumina brick, resulting in surface contamination. All of the above variations in surface finish had a substantial effect on background intensity and crack visibility in the differential absorption test.

5.2 DIFFERENTIAL-ABSORPTION TEST

The differential-absorption test was carried out using blaze orange microcapsules of 0.5 to 3.0 μm size (see Figure 18 for size distribution) and following the method described in Section 4.4. Coupons were then photographed on the faces and edges under black light using a Kodak K2 filter to reduce reflected ultraviolet (UV). The number of cracks per inch was measured from the photographs and is shown in Tables 11 and 12. On the specimens cut in warp and fill directions, cracks per inch were measured (the number of cracks intersecting a one-inch line) along the length or across the width of the specimen. For specimens cut at 45°, the two directions of measurement are as shown in Figure 24. Additionally, the intensities of crack indications and background fluorescence were estimated visually and rated on an arbitrary scale.

The crack patterns varied from highly visible (high crack intensity, low background) to indistinguishable. The most visible patterns were those faces with a smooth glassy surface layer. The less smooth coupons produced higher background intensity, sometimes obscuring the crack indications. In all coupons, the crack indications on the faces were aligned parallel to the warp and fill fiber directions, apart from those close to the edges of the 45° specimens (see Figure 24). Cracks on the edges of these coupons ran primarily in the thickness direction. Some edge cracks ran parallel to the specimen

47

Table 11. Differential Absorption Results for ACCRP Specimens.

|	Face A				Face B			
	Cracks/Inch		Intensity		Cracks/Inch		Intensity	
Specimen	Along (+45°)	Across (-45°)	Crack	B/G	Along (+45°)	Across (-45°)	Crack	B/G
ACCRP-3	(Not Visible)		L	M	20	17	M	L
-9	22	18	M	L-M	20	16	M	L-M
-10	13	10	M	M	9	8	H	L
-13	13	9	H	L-M	12	8	H	L-M
-16	10	7	H	M	8	9	M-H	M
-17	10	8	M	L	10	11	H	M
-22	8	11	M-H	L-M	10	10	H	M
-23	10	12	M	L-M	11	9	M	L
-24	10	11	H	M-H	11	12	M-H	M
-26	10	9	H	L-M	9	10	M-H	L
-28	8	11	M	L	(Not Visible)		M	M-H
-29	15	14	M	L-M	12	12	M	M
-32	10	10	M	L-M	11	9	M	M
-35	10	9	L	L	11	12	L	L-M
-38	16	12	M	M	15	12	M	M-L
-39	9	8	M	L	9	11	M	L-M
-43	11	13	L	L	7	8	L	L
-44	10	10	M	L-H	(Not Visible)		L	M
-47	10	11	M-H	M-H	11	10	M	M
-48	9	9	M	L	16	22	L	M

Note: Crack and background intensities are estimated on a comparative scale:

VL = Very Low
L = Low
M = Medium
H = High

Measurement directions on 45° specimens as shown in Figure 24.

Table 12. Differential Absorption Results for K650 Specimens.

	Face A				Face B			
	Cracks/Inch		Intensity		Cracks/Inch		Intensity	
Specimen	Along (+45°)	Across (-45°)	Crack	B/G	Along (+45°)	Across (-45°)	Crack	B/G
K650-66	13	14	M	L	14	16	L	L-M
-70	10	10	M	L-M	10	10	M	L-M
-71	14	16	VL-L	L	14	14	VL-L	L
-74	20	16	L-M	L-M	18	18	L-M	M
-75	20	22	L-M	L	18	24	L	M
-76	16	18	L-M	L-M	14	18	L-M	M
-77	12	12	L-M	L-M	11	11	M	M
-80	14	12	M	M-H	12	12	L	L
-81	13	13	M	M	13	13	M	L-M
-82	9	10	M	L-M	16	14	L	L
-83	9	9	M-H	L	11	11	M	L
-84	9	10	H	M	11	9	M	L-M
-85	9	7	L	L-M	11	7	L	L
-86	13	8	M-H	L-M	12	16	L	L
-90	13	12	M-H	L-M	20	12	M	L-M
-92	11	15	M-H	L-M	13	12	L-M	L
-93	11	13	M	L	12	14	VL-L	L-M
-99	12	11	M	L-M	13	13	M	L-M
-102	15	12	M-H	M-H	14	10	M	L
-107	12	14	M	L	16	16	M	L
-111	10	12	L	L-M	15	12	L	L

Note: Crack and background intensities are estimated on a comparative scale:

    VL = Very Low
    L = Low
    M = Medium
    H = High

Measurement directions on 45° specimens as shown in Figure 24.

Face A Before
Oxidation

Face A After
Oxidation

+45°

Face B Before
Oxidation

Face B After
Oxidation

+45°
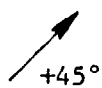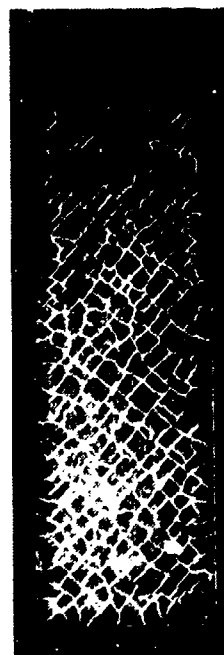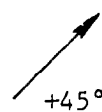
Figure 24. Differential Absorption Results, Specimen 16
Pre- and Post-Oxidation.

50

length and at midthickness; these correlated with delaminations seen in the coupons before coating.

Coupon 74 showed a pattern of highly visible cracks radiating from a surface-connected oxidation pit (see Figure 25). Coupon 3 (also Figure 25) showed a transition from closely spaced cracks at one end to an absence of cracks at the other end. The uncracked end showed a delamination zone in the coating; the coating had visibly begun to peel back from the substrate.

(a) Specimen 3 Showing Absence of Cracks at
    End Due to Coating Delamination.

(b) Specimen 74 Showing Cracks Radiating
    From Surface Pit

Figure 25. Differential Absorption Results,
           Specimens 3 and 74.

Figures 24 and 26 through 32 show a variety of the crack patterns before and after further oxidation testing of the coupons and typify the range of results observed. Note that there is little evidence of the effect of defects induced during the coating process. Average crack spacing is plotted in Figure 33 as a function of coating thickness.
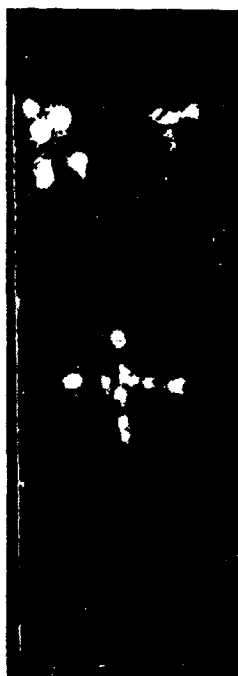
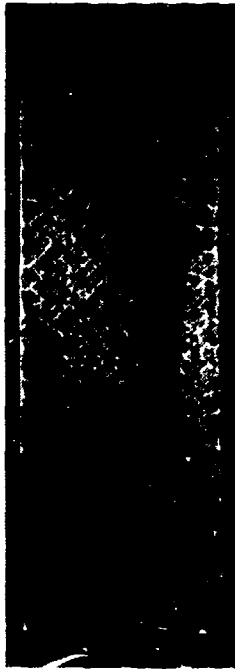Face A Before
Oxidation

Face A After
Oxidation
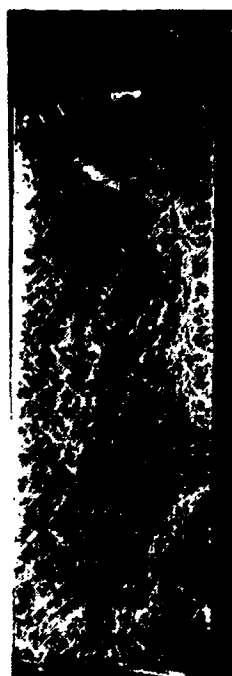
Face B Before
Oxidation

Face B After
Oxidation

Figure 26. Differential Absorption Results, Specimen
28 Pre- and Post-Oxidation.

Face A Before
Oxidation

Face A After
Oxidation

Face B Before
Oxidation

Face B After
Oxidation

Figure 27. Differential Absorption Results, Specimen
29 Pre- and Post-Oxidation.

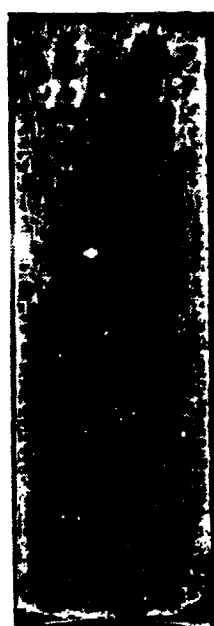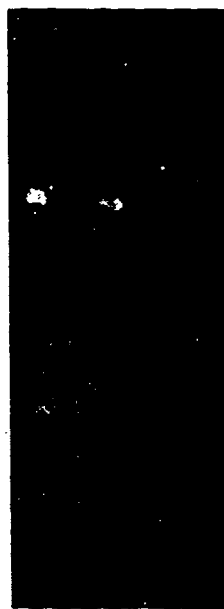Face A Before
Oxidation

Face A After
Oxidation

Face B Before
Oxidation

Face B After
Oxidation

Figure 28.   Differential Absorption Results, Specimen
70 Pre- and Post-Oxidation.

Face A Before Oxidation   Face A After Oxidation

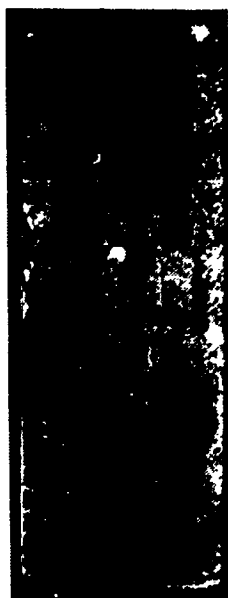Face B Before Oxidation   Face B Before Oxidation

Figure 29.   Differential Absorption Results, Specimen
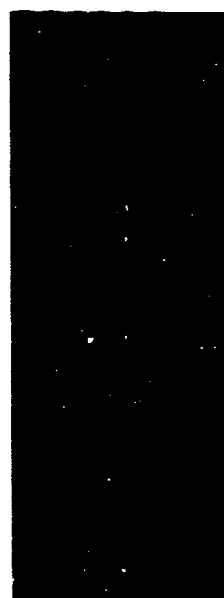77 Pre- and Post-Oxidation.

Face A Before
Oxidation
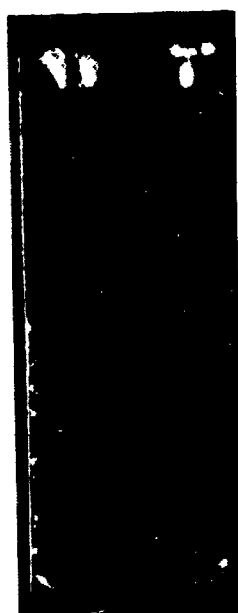

Face A After
Oxidation

Face B Before
Oxidation

Face B After
Oxidation

Figure 30.   Differential Absorption Results, Specimen
82 Pre- and Post-Oxidation.

Face A Before
Oxidation

Face A After
Oxidation

Face B Before
Oxidation
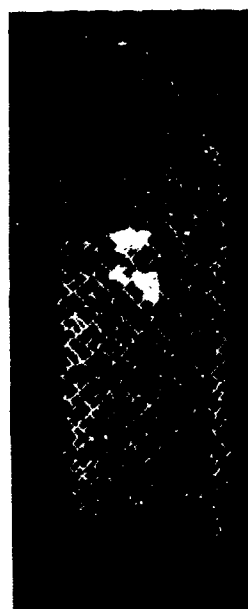
Face B After
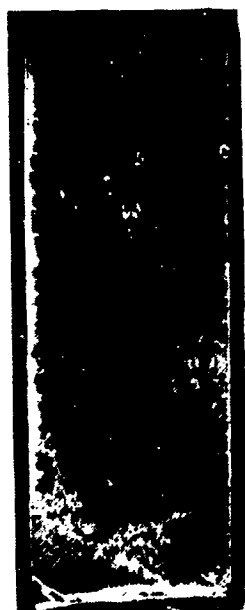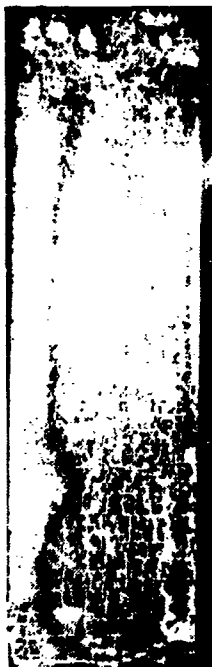Oxidation

Figure 31. Differential Absorption Results, Specimen
93 Pre- and Post-Oxidation.

Face A Before
Oxidation

Face A After
Oxidation

Face B Before
Oxidation

Face B After
Oxidation

Figure 32.   Differential Absorption Results, Specimen
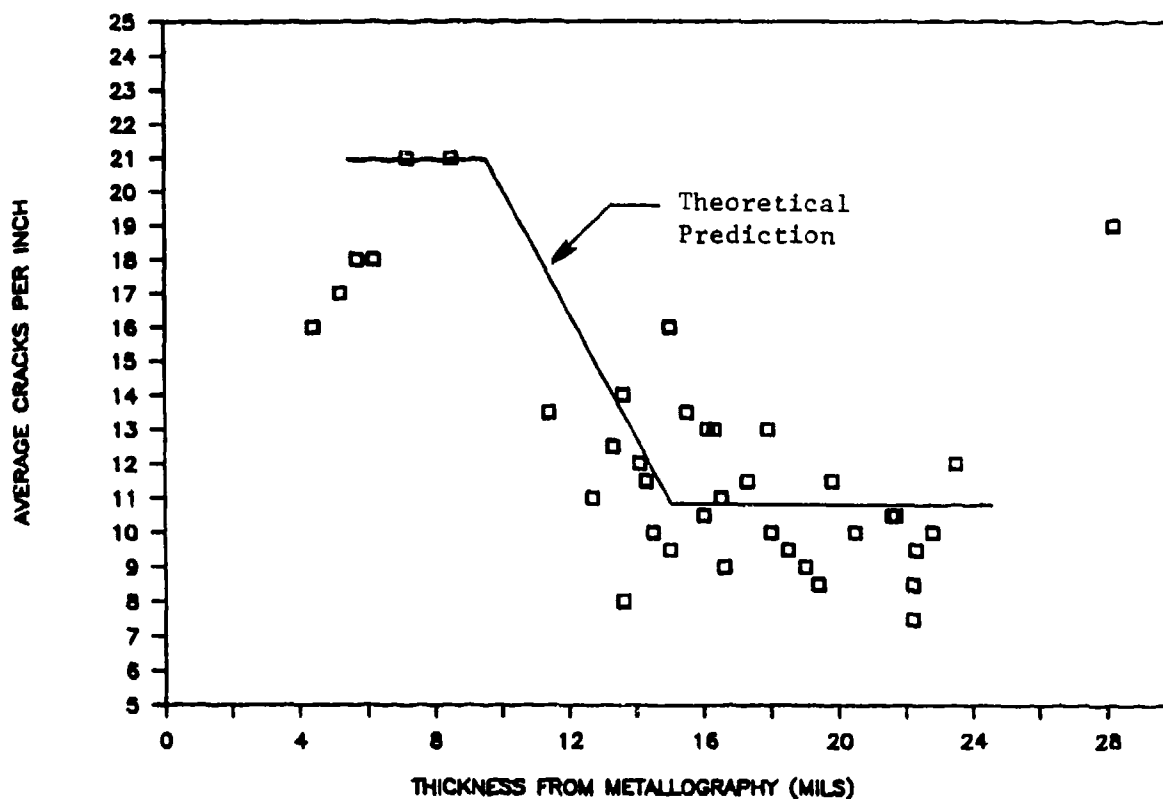102 Pre- and Post-Oxidation.

AVERAGE CRACKS PER INCH

25
24
23
22
21
20
19
18
17
16
15
14
13
12
11
10
9
8
7
6
5

0   4   8   12   16   20   24   28

THICKNESS FROM METALLOGRAPHY (MILS)

Theoretical
Prediction

Figure 33.   Average Crack Spacing as a Function of Coating Thickness.

5.3   INFRARED THERMOGRAPHY

Infrared (IR) testing was performed on a number of the coupons at this stage in order obtain feasibility data on the IR technique. The technique used a YAG laser operating at 10 watts continuous wave, with a 1.064-μm wavelength. Beam size was 2 cm high by 1 mm wide on the test coupon. The beam was swept across the coupon at a rate of approximately one inch per second. Figure 34 shows scan results from Coupon 71, with the beam sweeping from right to left. Figure 34b shows local heating around a surface oxidation pit (top center). Figure 34c shows a smaller but similar feature (left center). Both features could be seen, by visual examination, to penetrate the coating.
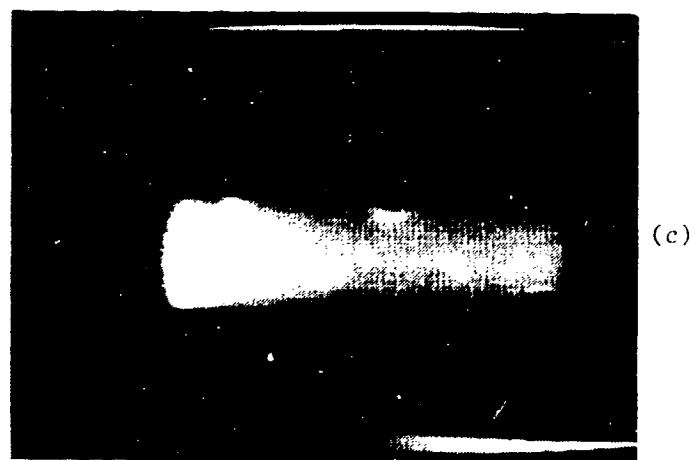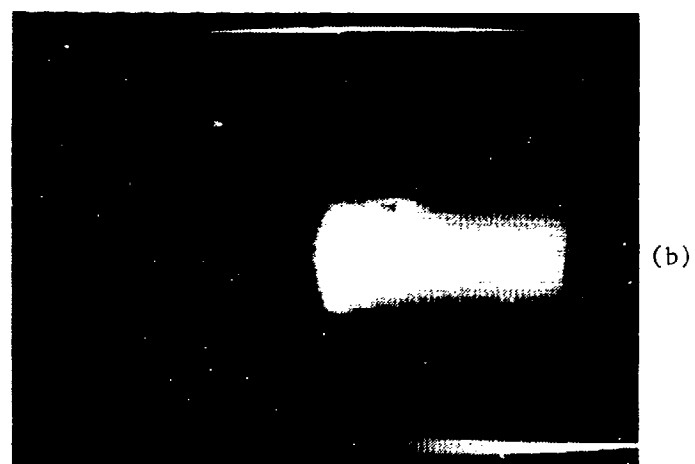
Figure 34. Infrared Scan of Specimen K650-71.

6.0 MODEL OF CRACK DEVELOPMENT

6.1 ANALYTICAL APPROACHES

The objective of this study was to develop an analytical procedure for predicting the occurence of cracks in coated carbon-carbon materials. This was necessary to elucidate the crack patterns encountered during differential-absorption testing.

Two analytical approaches were adopted. The first approach was based on the one-dimensional, shear-lag model used for preliminary estimations and parametric studies. The second approach used a more rigorous finite-element model that was considered more realistic in modeling the geometry and biaxial stress effects.

6.2 CRACK ANALYSIS BY SHEAR-LAG MODEL

The classical shear-lag model provided a simple and useful analytical approach for predicting coating behavior during temperature variation. Figure 35 shows a single-phase layer in the process of cooling down and cracking. The reducing crack interval is designated by 2L.

Initially, 2L was taken to be the entire uncracked coating length. Since the coating was applied on the upper and lower surfaces of the component, only the top half was modeled due to the geometric symmetry. Using the classical shear-lag theory and considering thermal effects, the induced coating thermal strain was found (Reference 3) to be:

$$\varepsilon_{2_m} = \varepsilon_0(\cosh \mu x/\cosh \mu L - 1)$$

Where

$$\varepsilon_0 = (\alpha_2 - \alpha_1)\Delta T/(1 + E_2 h_2/E_1 h_1)$$

$$\mu^2 = \frac{G}{(h_1 + h_2)} \left(\frac{1}{E_1 h_1} + \frac{1}{E_2 h_2}\right)$$

$$G = \frac{G_2(h_1 + h_2)}{(h_2 + h_1 G_2/G_1)}$$

ε_0 is the induced coating strain at the middistance between two adjacent cracks, and $(\cosh \mu x/\cosh \mu L - 1)$ is a strain-distribution factor. The thermally induced strain peaks at the middistance between cracks and gradually diminishes toward the cracks; α_1, α_2, E_1, E_2, G_1, G_2, h_1, and h_2 are the thermal expansion coefficients, Young's moduli, shear moduli, and thickness values, respectively. The subscripts, 1 and 2, denote the corresponding material systems. Both the substrate and the coating materials are assumed to be isotropic.
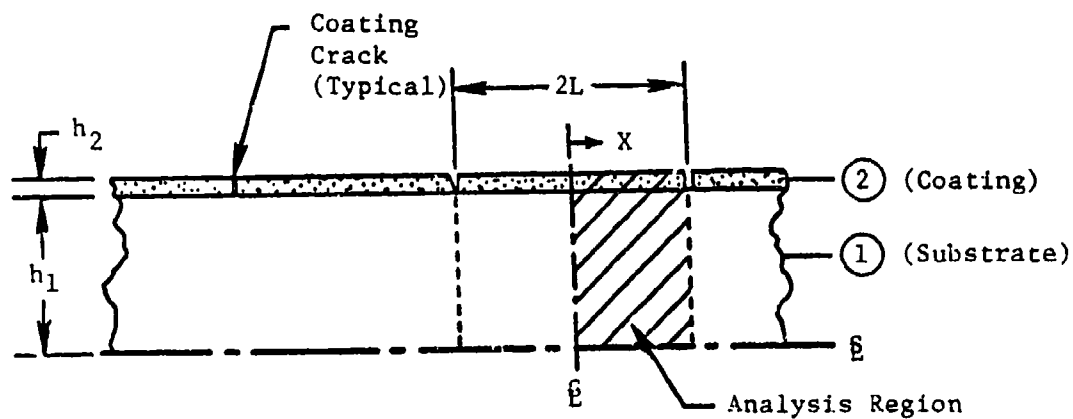
(a) Model for Shear-Lag Analysis

0.006 in. (ACCRP)
0.002 in. (K650)
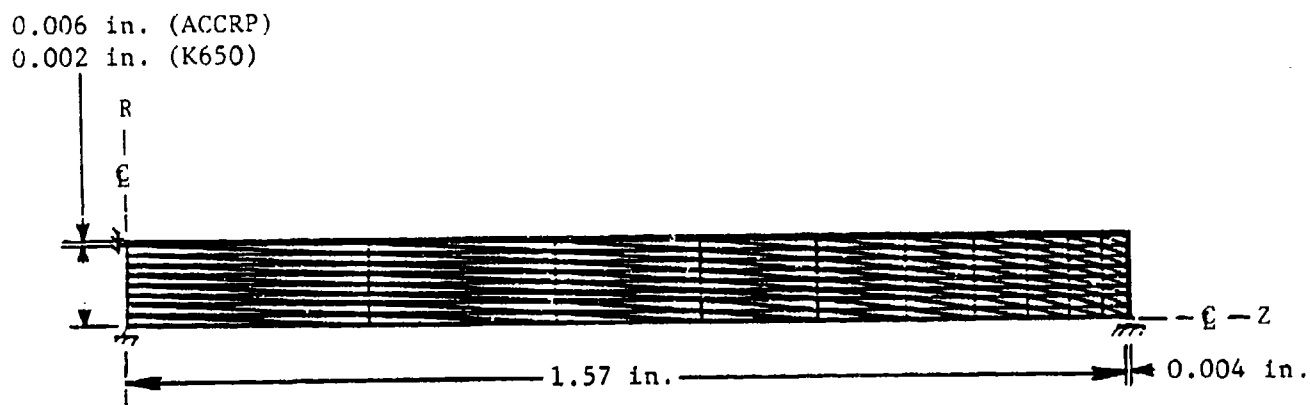
Dimensions of a Quarter Specimen

Stress-Free Temperature   2400° F

Cool-Down Temperature   70° F

	Substrate	Coating
Modulus of Elasticity, E (10^6 psi)	16	30
Poissons Ratio μ	0.28	0.19
Coefficient of Thermal Expansion $\alpha(10^{-6}/°\text{ F})$	0.5	2.8
Allowable Thermal Strain	-	0.0067

(b) Dimensions and Materials Properties Used

Figure 35. Specimen Model for Shear-Lag and Finite-Element Analysis.

Based on the above equations, induced thermal strain can be calculated for a specified temperature change, ΔT. If the induced strain exceeds the allowable strain value, an additional cracking event is assumed to occur at the middistance between the existing cracks. The process continues until the component reaches the final temperature.

With the expression of induced coating strain, the development of crack density, crack spacing, and maximum coating strain during cool-down can be calculated and plotted. Furthermore, by changing the coating thickness, a parametric study can be made. The temperature at which the coating develops the first crack can be found for the different coating/substrate thickness ratios. If the component remains uncracked at the final temperature, the residual strain and a margin of safety can also be calculated for different coating/substrate thickness ratios.

6.3 CRACK ANALYSIS BY FINITE-ELEMENT MODEL

A two-dimensional, finite-element model was used for the thermal stress analysis of coated components by the application of the GE finite-element computer program CYANIDE. The component was analyzed by taking account of the section geometry and the in-plane stresses. The plane stress condition was assumed. A preprocessor was developed to facilitate the generation of finite-element models (with or without cracks).

The computed strains were compared with the allowable strain value for the prediction of new crack developments. The developed cracks were then simulated in the subsequent finite-element model for further thermal stress analysis. The process was continued until the final temperature was reached. Only the opening mode cracks that were perpendicular to the interface were considered. The interfacial cracks were beyond the scope of this study.

6.4 MODEL RESULTS FOR LTV MATERIALS

The crack pattern development for the two coated specimens of ACCRP and K650 material systems were predicted by the analytical procedure presented in this report. Dimensions, thermal loads, and material properties of those two specimens are shown in Figure 35. Where possible, measured values were used. For strain to failure and coating modulus, values had to be estimated as measurement was not practical.

For the crack analysis by the shear-lag model, the input data file was built using the data shown in Figure 35. The development of the crack density and the induced coating strain for the ACCRP specimen re predicted as shown in Figures 36 and 37, respectively. The allowable cc ing thermal strain was estimated to be 0.00067 based on the coating fracture strength.

During the cool-down process, the induced coating strain grows gradually. Once the coating strain reaches the allowable value, cracks initiate and develop rapidly. Between successive cracking events, the coating strain
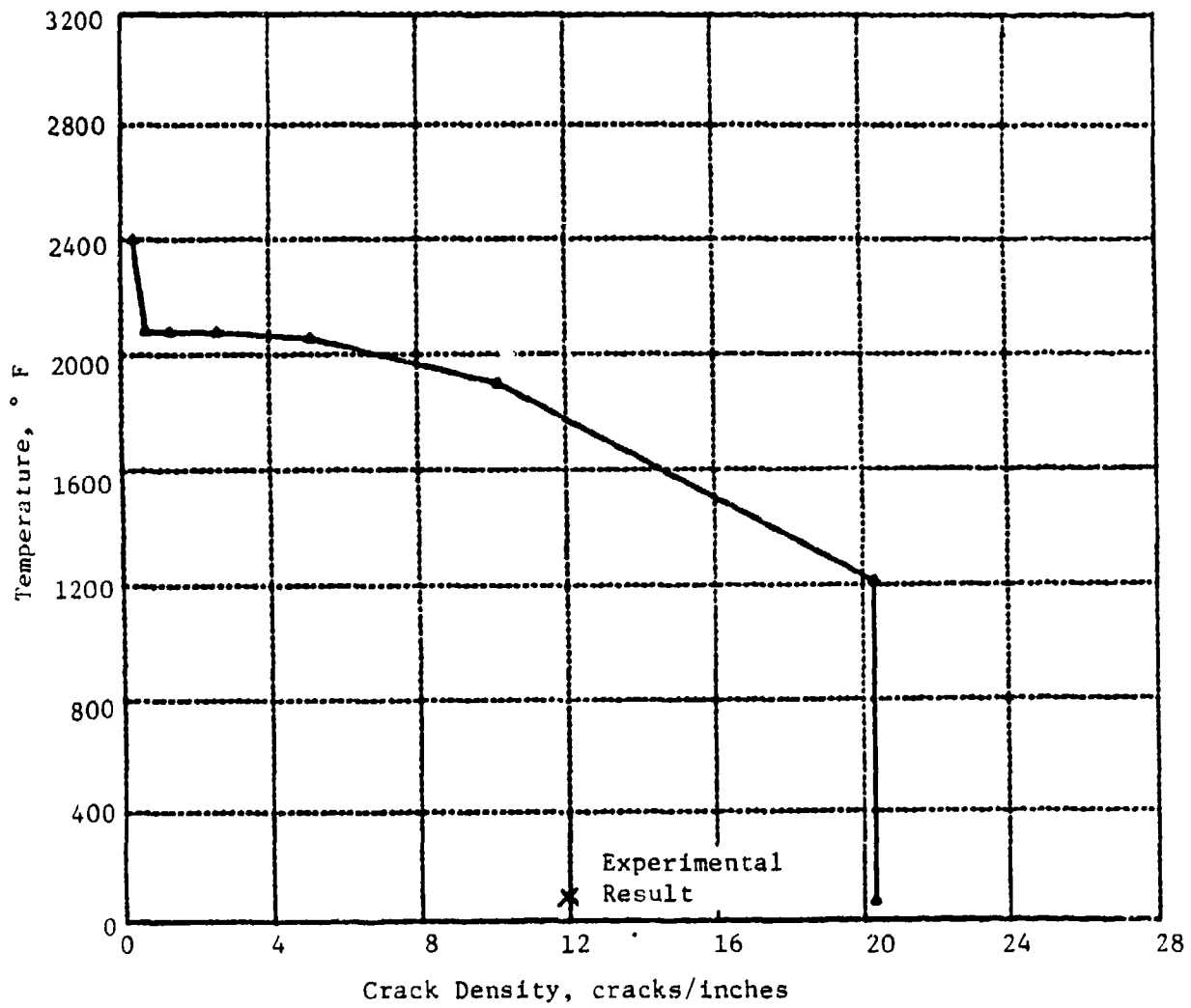
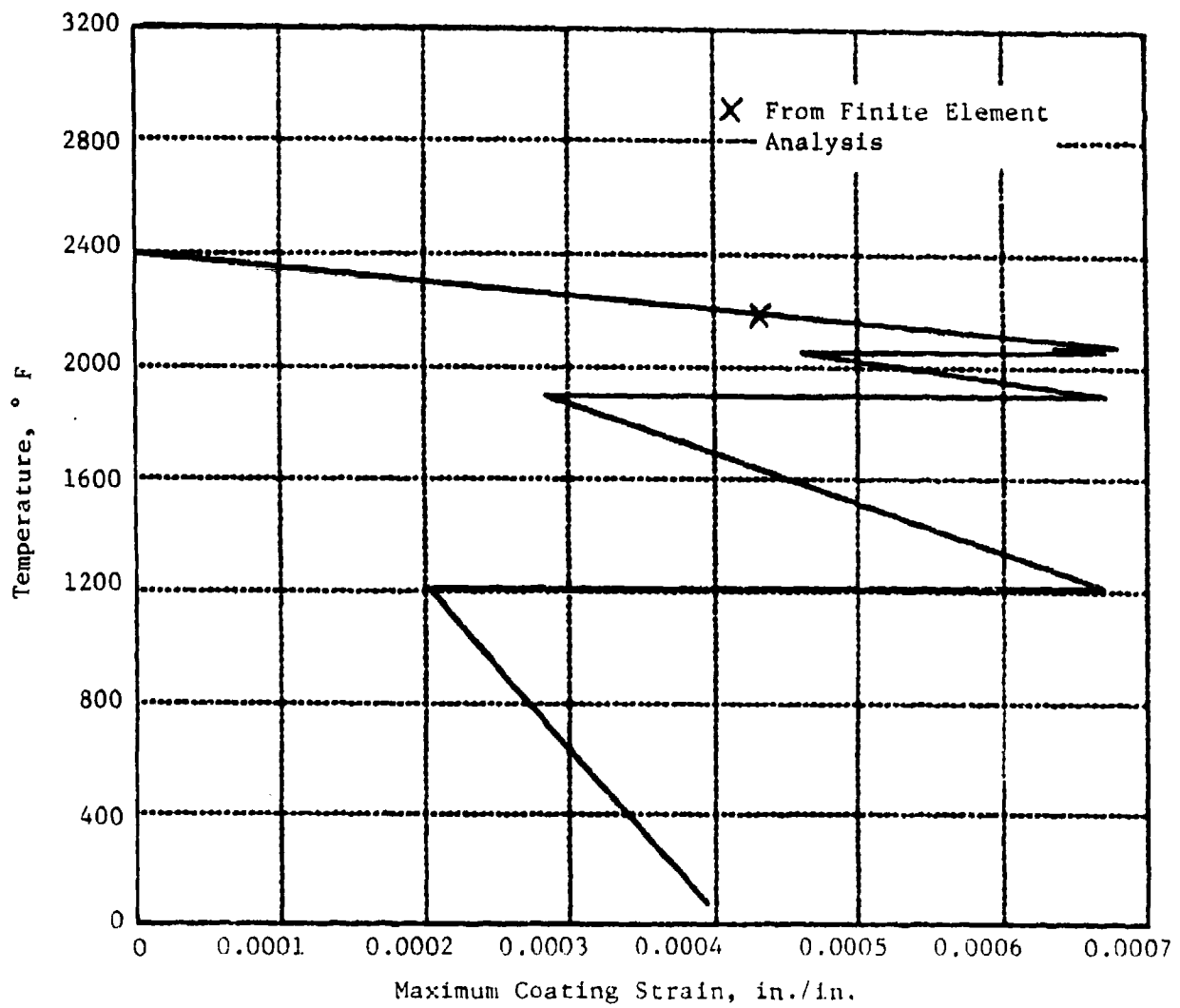Figure 36. Predicted Crack Density During Cool Down.

Figure 37. Strain Variation During Cool Down.

increases linearly. If the coating/substrate thickness ratio is increased, the temperature for developing the initial coating crack will be decreased. The coating strain decreases (or the margin of safety increases) in proportion to the increase of the coating/substrate thickness ratios.

Figure 33 shows the prediction of crack spacing as a function of coating/ substrate thickness ratio, and experimental values are plotted for comparison. The experimental results are scattered about the theoretical prediction. This data scatter is expected and is probably a result of variability in coating properties. Note also that the metallography results showed interfacial cracks that were not considered in the model, and these are likely to cause some discrepancy.

6.5 CONCLUSIONS FROM MODEL

Based on the predictions of coated ACCRP and K650 specimens by the developed analysis procedure, the following conclusions were reached:

1. The stress induced in the coating was in tension and that in the substrate was in compression during the thermal cool-down process. The coating was cracked at the temperature when the tensile stress/strain became critical.

2. Induced thermal stress/strain was proportional to temperature drop from the stress-free temperature at which the coating material was applied to the component. Analytical predictions correlated reasonably well with the experimental results; thus, it is recommended that the shear-lag model be used for the preliminary estimation or the parametric study of the coating crack patterns.

3. It is a relatively complicated problem to predict the crack behaviors in coated components. In addition, to derive the precise relationship among contributing parameters, accurate thermo-physical and mechanical properties of the substrate and the coating layers should be available. The present work was a preliminary prediction of the coating crack developments during the thermal cool-down process. Further work is suggested for the prediction of interfacial/interlaminar cracks and three-dimensional effects on the crack pattern developments.

7.0 SEALANT EVALUATION AND OXIDATION TESTS

7.1 OXIDATION INHIBITOR

The materials tested as oxidation inhibitors were boron, boron carbide, and a glass containing B_2O_3, BaO, K_2O, and TiC. The boron was purchased as a powder, particle size 0.15 μm, and the boron carbide was bought as a 0.04 μm powder. Both powders were microencapsulated with approximately 50% loading in the microcapsules. Microcapsule size was determined by SEM to be 0.25 to 1.0 μm in diameter. The glass was milled to a size range of 0.5 to 5.0 μm.

7.2 INHIBITOR APPLICATION

Eight coated coupons were selected for the oxidation test, of which two were untreated and run as control samples, and each sealant composition was applied to two coupons. The coupons were selected to have estimated coating thickness in the range of 0.011 to 0.016 inch and no defects indicated by prior NDE tests. The coupons were first held at 1100° F for 1 hour in order to remove any traces of dye microcapsules that might prevent sealant from entering the cracks. The sealants were each suspended in isopropyl alcohol with a concentration of 50 g/liter and were applied by dipping the coupon in the suspension and allowing it to drain. The original intention had been to apply the sealant at the same time as the fluorescent dye; however, this was not pursued because the sealant powder colors obscured the dye indications. Examination under a microscope confirmed that all three sealants were seating preferentially in the surface cracks. Table 13 shows the coupon treatments.

Table 13. Test Specimen Treatments and Oxidation Life.

Specimen	Treatment	Hours to 5% Weight Loss
ACCRP-16	Boron Carbide	12.5
ACCRP-28	Glass	11.8
ACCRP-29	No Treatment	18.0
K650-70	Boron	20.2
K650-77	No Treatment	12.8
K650-82	Glass	20.7
K650-93	Boron Carbide	10.4
K650-102	Boron	15

7.3 OXIDATION TESTING

The eight coupons were then dried, weighed, and exposed in a furnace under the oxidation cycle described in Table 14.

Table 14. Oxidation Test Cycle.

2 hours at 2400° F	Cool and Weigh
2 hours at 2000° F	Cool and Weigh
16 hours at 1500° F	Cool and Weigh
2 hours at 2400° F	Cool and Weigh
16 hours at 1200° F	Cool and Weigh

Coupons were removed from the test as soon as weight loss exceeded 5%. The results of the oxidation test are plotted in Figure 38. The data were interpolated to estimate the time to 5% weight loss. The times are shown in Tables 13 and 15.

Table 15. Summary of Oxidation Results.

Treatment	Hours to 5% Weight Loss
Boron Carbide	11.45
Control (Untreated)	15.4
Glass	16.25
Boron	17.6
(ACCRP Substrate)	(14.1)
(K650 Substrate)	(15.8)

It is concluded, bearing in mind the small number of samples, that there was no clear advantage gained by any treatment system. The boron-treated samples showed the longest life, but this was only 2.2 hours longer than the average for the untreated samples and may easily have resulted from random variation. Any effect of the treatment would have to be major in order to show on this kind of test. A concern before the test was that the difference in substrate materials would seriously affect the oxidation lives. The test results showed that the average lives for AACRP and K650 substrate specimens differed by only 1.7 hours.

7.4 POST-OXIDATION NDE TESTS

The oxidation tested samples were then examined by CT radiography. It can be seen from the results shown in Figure 7 that there were two primary routes of oxidation failure. Coupons 16, 28, 70, 77, and 82 showed the major loss of material immediately under the coating and fairly evenly distributed over the interface, suggesting a failure mechanism of uniform oxygen infiltration through the coating. Coupons 29, 93, and 102 showed loss of material
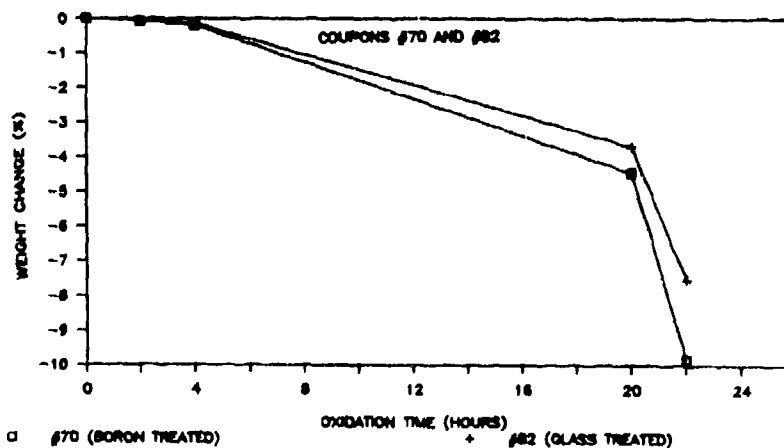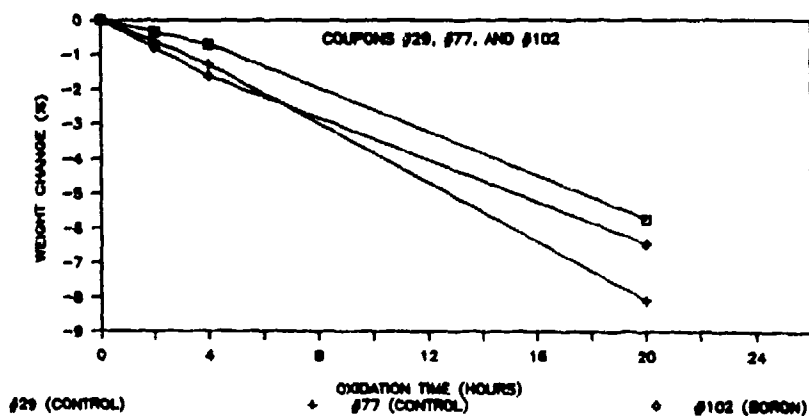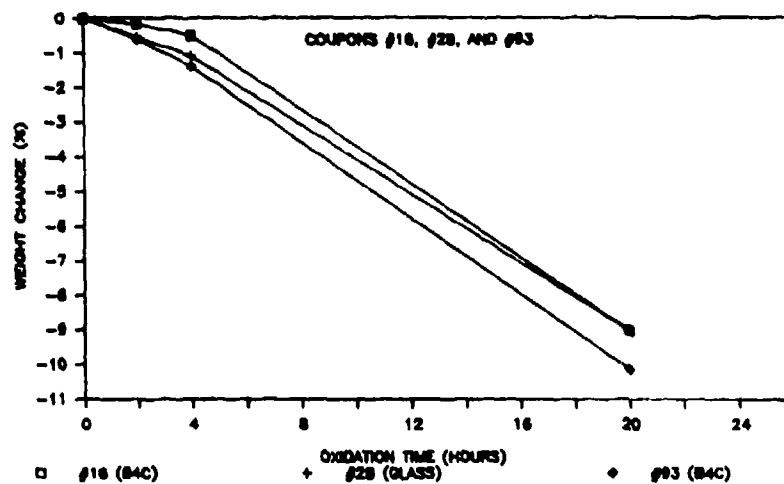
68

Figure 38.   Specimen Weight Change During Oxidation Tests.

along the midplane, with evidence of large voids next to the edge of the coupon. The mechanism of oxidation is most likely through the coating on the edge of the coupon.

The coupons were also evaluated by means of the eddy current technique described in Section 3.4. The results in Table 16 illustrate the change in eddy current signal resulting from the oxidation test. In all cases, the eddy current signal is reduced, indicating a reduction in material conductivity.

Table 16. Eddy Current Readings Pre- and Post-Oxidation.

	Face A			Face B		
Specimen	Before	After	% Change	Before	After	% Change
16	5.45	4.52	-17.0	5.16	4.71	-8.7
28	5.47	4.84	-10.7	5.01	4.37	-12.7
29	5.40	4.76	-11.8	5.39	5.04	-6.5
70	4.61	3.68	-20.0	4.58	4.34	-5.2
77	4.58	4.20	-8.3	4.28	4.04	-5.6
82	4.49	3.97	-11.6	4.68	3.61	-22.0
93	4.76	4.44	-6.7	4.78	4.38	-8.3
102	4.73	4.49	-5.0	4.76	4.39	-7.7

Note: Readings are instrument output in volts. Measurements taken at center of each face.

7.5 POST-OXIDATION DIFFERENTIAL ABSORPTION

The differential absorption test was performed on the coupons after oxidation testing. The results are shown in Figures 24 and 26 through 32. Points of interest are as follows:

1. Crack patterns and density may vary from the preoxidized state. Coupons 16, 29, 77, 93, and 102 all showed essentially the same crack pattern after oxidation, although a few new cracks did appear. Coupon 28 showed many more cracks after oxidation. Coupons 70 and 82 exhibited fewer cracks, with new large uncracked areas. These corresponded to areas where the coating was visibly delaminated from the substrate.

2. Crack patterns were generally more clearly visible in the differential absorption test. Crack intensity was higher and the background less bright.

3. The surface appearance indicated that the glaze layer seen before oxidation was now missing.

70

8.0 METALLOGRAPHY

Metallography was performed on 20 oxidized coupons. Magnification levels were set at 5× for full cross-sectional coverage and 100× for centerline thickness measurements. Each coupon was evaluated for coating thickness at the center cross section only.

8.1 METHOD

Oxidized coupons were prepared for metallography as follows:

a.   Coupons were sliced at the approximate center using a slow-speed diamond wheel saw. Some minor chipping at the edges could not be avoided due to the brittle nature of the coating.

b.   Coupons were then mounted in epoxy using a vacuum-impregnation technique. This ensures that no air pockets or bubbles will form in the epoxy during cure. Some cracking of the epoxy may be found in areas that cured disproportionately quickly.

c.   Epoxy-mounted coupons were then rough ground down to the cross section surface and, if necessary, down past where any surface chipping may have occurred.

d.   Final polishing was performed using 3-μm diamond paste.

e.   Identification and orientation were scribed into the epoxy mount for traceability.

8.2 COATING THICKNESS MEASUREMENTS

Metallographic montages, produced at either the top or bottom center of each coupon evaluated, covered approximately 0.12 inches of the coating/substrate boundary. Figure 15 is a typical montage. The coating/substrate boundary was somewhat clarified by offsetting the focus slightly. This was due to the preferential polishing of the lower resistance substrate material over the hard coating layer. The outline of the conversion layer is also shown in Figure 15.

Measurements of coating thickness were performed on each montage at five equally spaced stations. Care was taken not to bias the results by placement of the measurement stations. Coating thickness was defined to be the distance from coating surface (excluding "bubbled" material and surface contamination) to the last incidence of coating material along the line of the measurement station. If the coating material was erratic (that is, there was substrate material evident along station path), then the distance of substrate initially included was deleted from the measurement. The average of the five measurements was listed as the coating thickness. These values may be found in

71

Tables 7 and 8. Figures 39 and 40 illustrate delaminations in the materials. Figure 41 shows the internal voids resulting from thermal cycling of Specimen ACCRP-16, and Figure 42 shows CT images of the same sections. Note that the internal cavity is filled with epoxy from the mounting process; it can be identified by the presence of cracks. Figure 43 shows the development of interlaminar cracks and substrate oxidation in the same specimen.
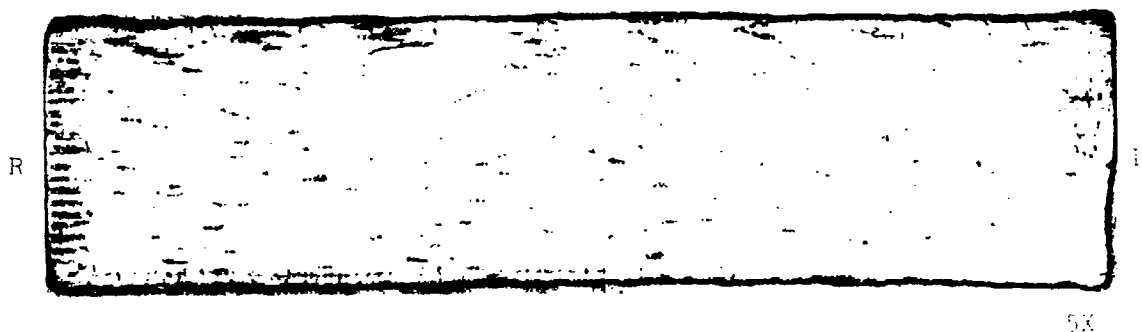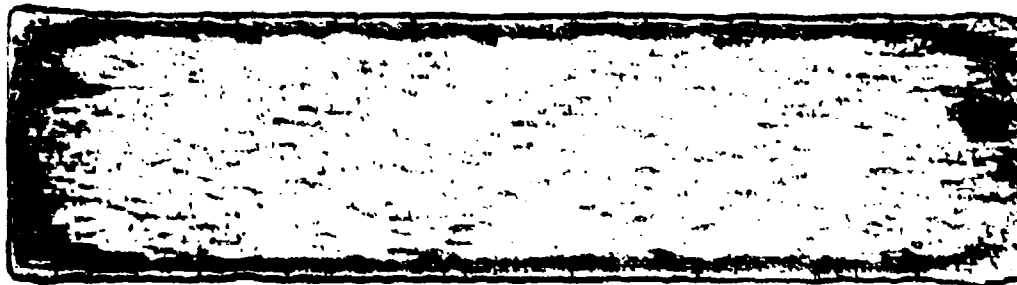

(a) Center Cross Section of Specimen K650-80
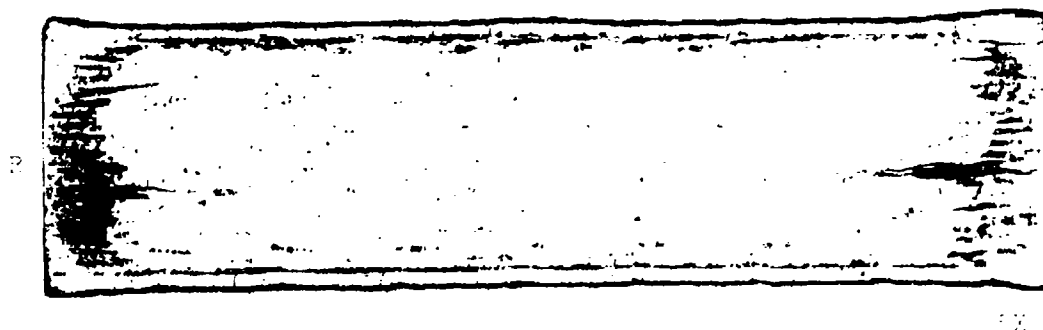
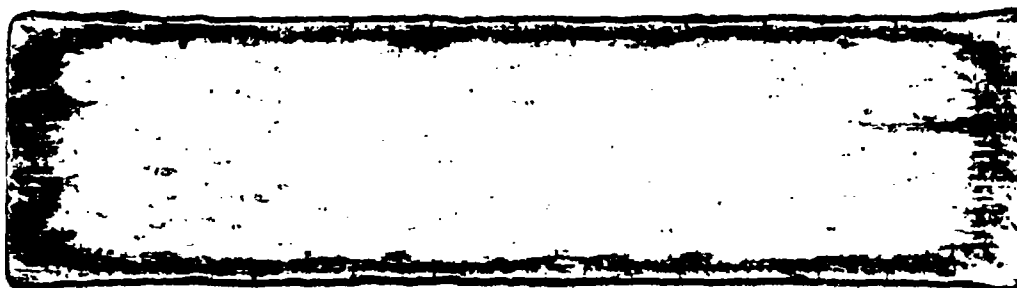(b) Center Cross Section of Specimen ACCRP-24

Figure 39. Metallographic Cross Sections of Thermally Exposed Coated 2D C-C Coupons 24 and 80 (1-Hour Heat Soak).
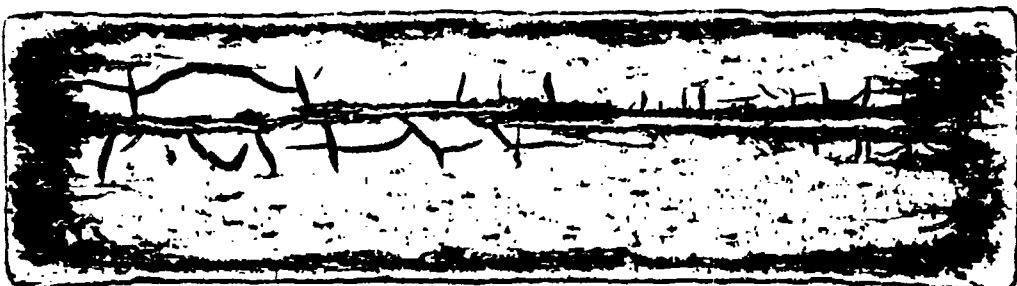
Figure 40. Metallograph of Delamination and Edge Coating Boundary.

25X

73
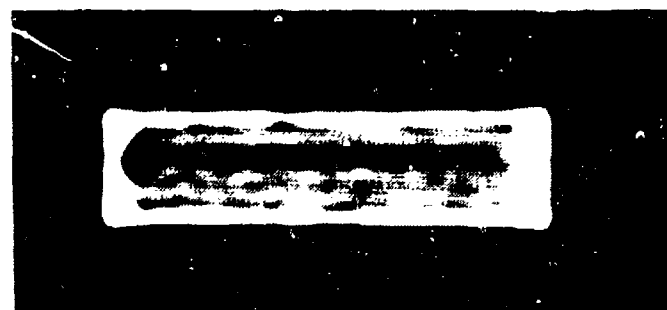
(a) Cross Section 0.5 inch From Reference End

(b) Cross Section 1.5 inch From Reference End

(c) Cross Section 2.5 inches From Reference End

Figure 41. Metallographs of Specimen ACCRP-16
After Oxidation Testing.
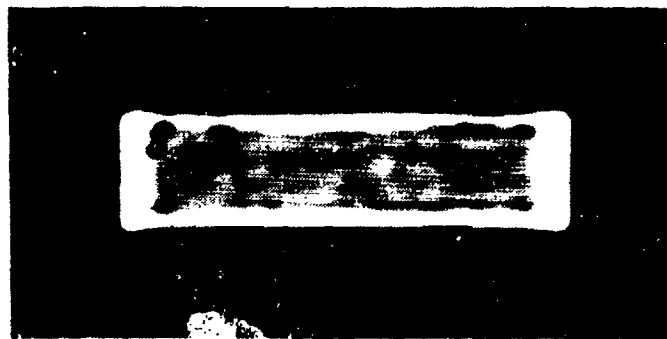
Note: Same Sections Shown
Metallograpically
in Figure 41.

Figure 42. X-ray CT Cross-Sectional Images of Specimen
ACCRE '6 Af er Oxidation Cycle.

Cracks Developed in Epoxy
(Not Material Related)

Voids Created by Substrate
Oxidation (Epoxy-Filled)

Figure 43. Metallographic Evidence of Substrate Oxidation in Specimen ACCRP-16.

76

9.0 ADDITIONAL MATERIALS

9.1 MATERIAL DESCRIPTION

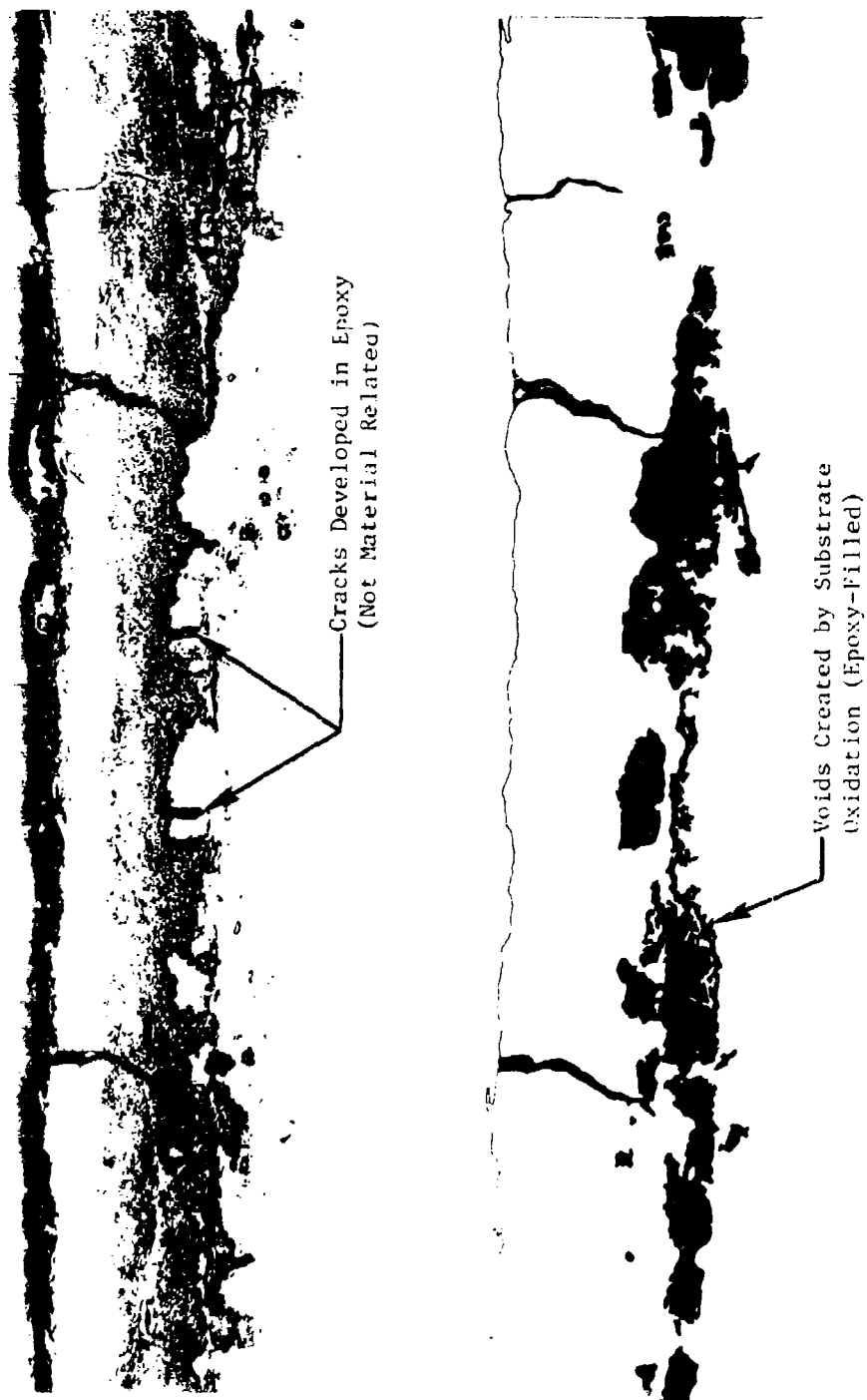Differential Absorption and CT Radiographic tests were performed on coupons of two additional material systems. One set of 21 coupons consisted of SAIC II inhibited matrix substrate with San Fernando Labs (SFL) Mod IV coating. Coupon size was 2×0.75×0.125 in. The coupons had been coated in three batches with process variations introduced to give a range of layer thicknesses. The coating consisted of a nominally 0.004-inch thick conversion layer with two interlayers and an outer layer of silicon carbide approximately 0.01-in. thick. The inhibited matrix substrate had silicon carbide, zirconium diboride, and boron carbide added to the matrix.

The second set of 20 coupons consisted of Chromalloy coating on GAT substrate. Coupon size was 3.25×1.25×0.2 in. The coating was an applied boron-containing sealant layer with a 0.01 to 0.012-inch thick silicon carbide overlayer.

Both substrate/coating systems were representative of materials envisaged for future gas turbine applications. These systems differ significantly from the LTV materials in the addition of oxidation-inhibitors to the substrate matrix and in the coating which had chemical vapor deposited (CVD) layers in addition to the conversion layers. The surface finish was less smooth than that of the LTV coating, and in particular the Chromalloy coating showed a very irregular surface.

9.2 DIFFERENTIAL-ABSORPTION TEST

Differential-absorption testing of the Chromalloy coated coupons showed no visible fluorescent indications (see Figure 44). Microscopic examination showed the presence of cracks with width in the range of 3 to 10 µm. This crack width should be suitable for detection with the 0.5 to 3 µm dye particle size used. It is possible that the cracks did not penetrate sufficiently deep to provide an absorption path for the dye-carrying fluid.

Fluorescent indications on the SFL coated coupons varied from nonexistent to faint. Figure 44 shows the coupons with the most visible indications.

9.3 CT RADIOGRAPHY

Typical CT radiographic test results from the two sets of coupons are shown in Figures 45 and 46. CT results from both materials exhibit similar features as follows.

The average CT numbers were much higher than for the noninhibited matrix LTV coupons. CT numbers ranged from 500 to 2500 compared to a range of 370 to 410 for the LTV material. The variation in CT numbers within a coupon was

(a) Specimens with SFL Coating
on SAIC Substrate

(b) Specimen with Chromalloy on
GAT Substrate

Figure 44.   Differential Absorption
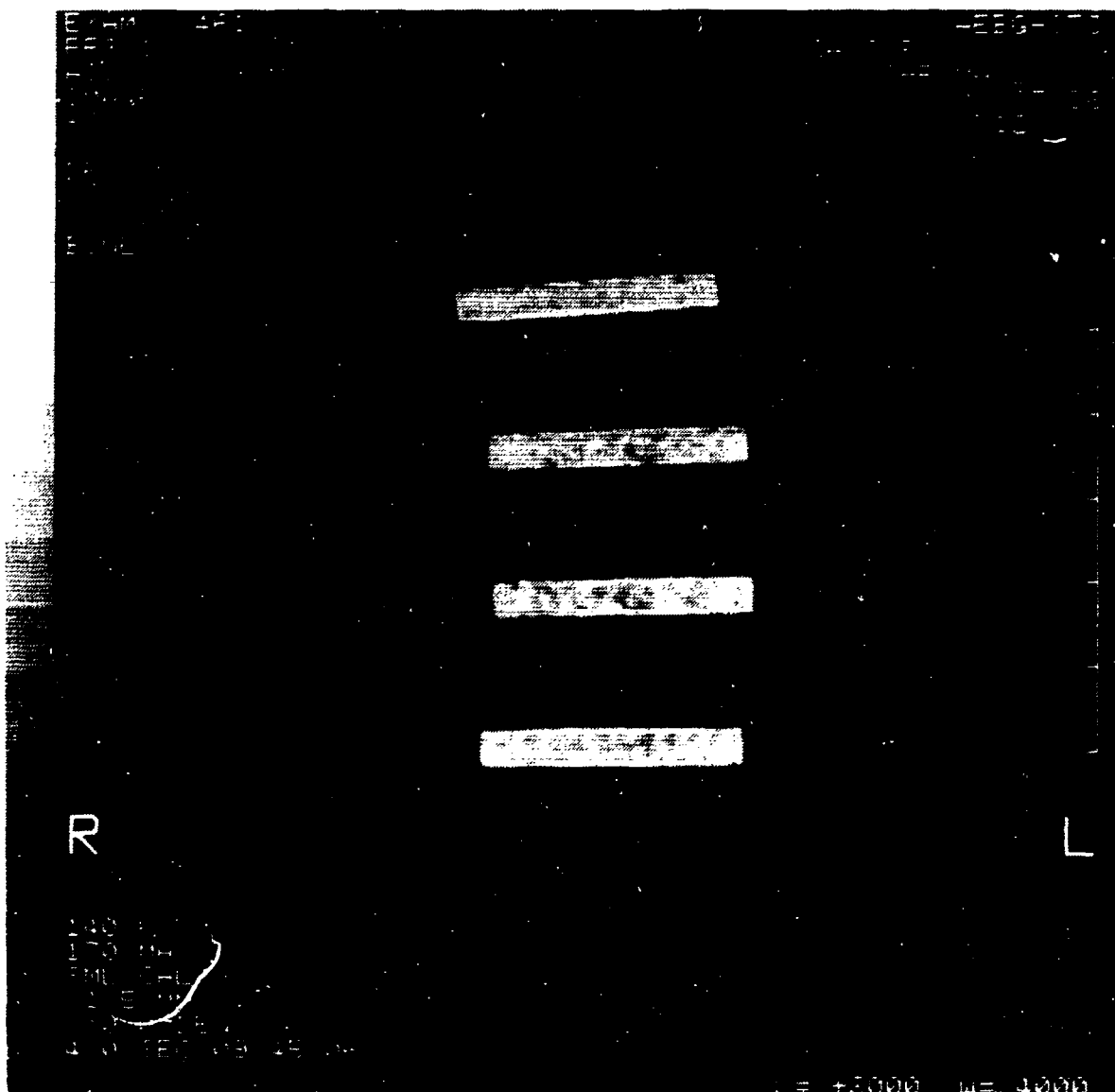Results on SFL and Chromalloy
Coated Specimens.

Figure 45. X-ray CT Images of Chromalloy Coating on GAT Substrate Coupons.
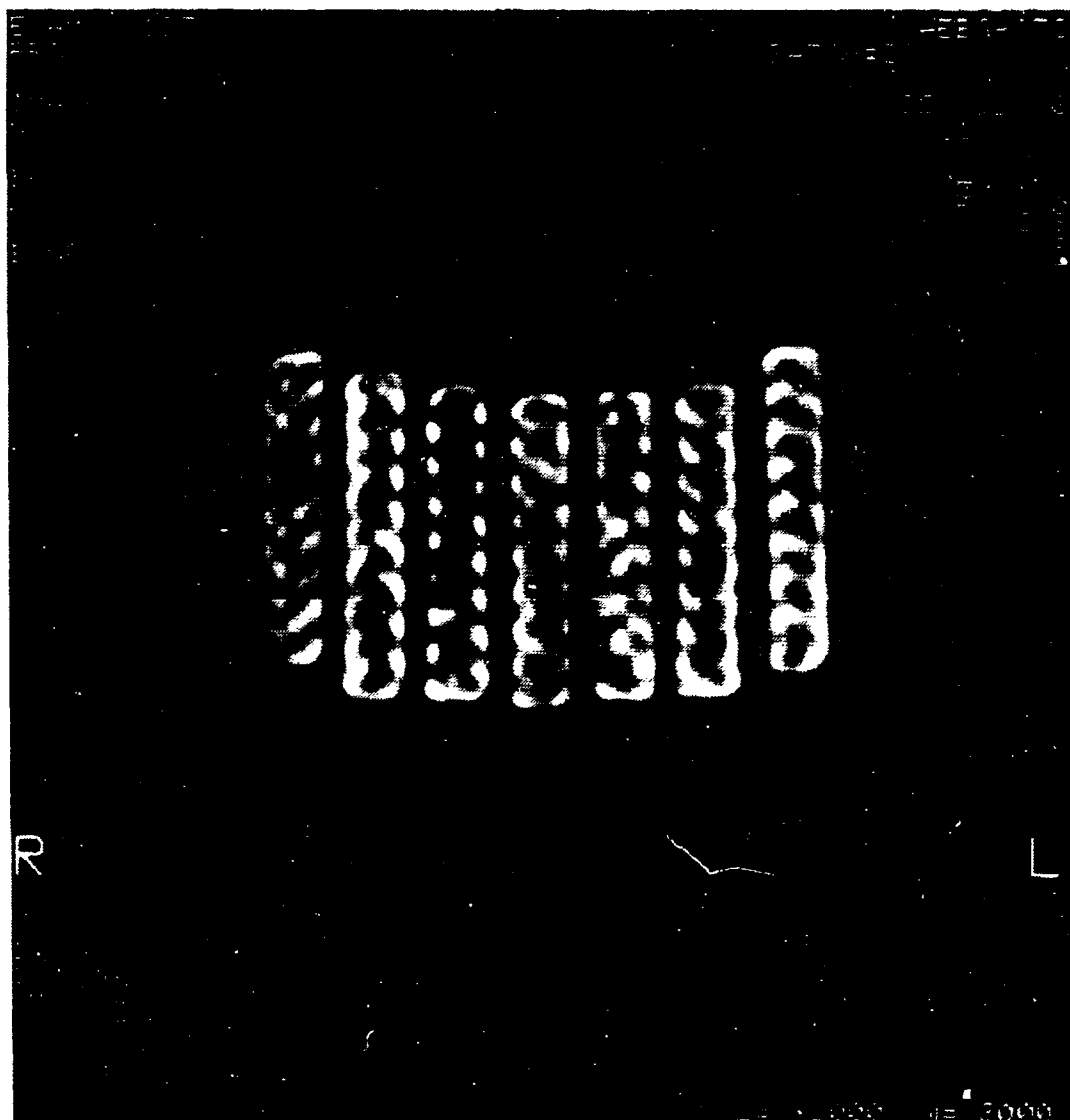
Figure 46. X-ray CT Images of SFL Mod IV Coating on SAIC Substrate Coupons.

also much higher for the inhibited matrix material, and the photographs showed a regular pattern of variation. These results were consistent with the distribution of elements with high atomic number (such as zirconium) that were present in the matrix and therefore located in the interstices of the carbon weave. Note also that the coating was not clearly evident in the images because there was not a contrast between CT number of substrate and coating as there was for the LTV coupons.

10.0 DISCUSSION

10.1 DIFFERENTIAL ABSORPTION TEST RESULTS

A primary concern is to assess coating quality, and the differential-absorption method was suggested to achieve this. The program results have demonstrated that the method is effective in detecting coating cracks, though detectibility is highly influenced by surface condition. However, the surface cracks are a normal feature of the coatings studied, so the problem becomes one of distinguishing "normal" cracks or crack patterns from those which indicate abnormal conditions. Some abnormal conditions can be detected, such as very thin coatings, which produce a closely spaced crack pattern, and actual results fitted well with theoretical predictions. The dependence of crack spacing on thickness is not a reliable thickness measurement other than to indicate very thin coatings, and there are alternative and better ways to measure coating thickness.

Another feature which may be detected by the crack pattern is oxidation damage under the coating. This was observed in the specimens which had been through the oxidation cycle. On some surfaces, lack of cracks corresponded to coating delamination, as might be expected. However, other specimens had major subsurface oxidation damage which did not result in any changes in the crack pattern. Alternative methods such as CT radiography and eddy current can be used to detect this type of damage, and CT radiography in particular gives a more accurate and comprehensive indication.

The above remarks apply primarily to the LTV coatings and noninhibited substrates. Coated carbon-carbon is in a state of development, and future material systems for gas turbine engines might be very different. It is conceivable that the onset and growth of coating cracks may be an indicator of coating deterioration in future systems, and the differential-absorption method would then be potentially very useful. Loading of oxidation inhibitors in the substrate can make the eddy current and CT radiography tests less reliable, so differential absorption may offer an alternative.

The present conclusion is that the differential absorption method could not be used as a primary NDE method to indicate coating quality. Other NDE methods can provide the same information more directly and damage conditions do not necessarily affect the differential absorption results. The method should be considered a useful supplementary test, especially in view of ease of application, and may meet the requirements of newer material systems.

The addition of glass-forming materials to the differential absorption fluid did not have a major effect on the oxidation life. Any small gain in oxidation-resistance would be masked by the variability in survival time of untreated specimens. A much larger number of samples would be needed to produce conclusive results. The amount of sealant material introduced in this experiment was very small, and it may be more rewarding to paint or deposit sealants onto the surface to give 100% coverage.

10.2 EDDY CURRENT TEST

The eddy current test was considered as a potential means to measure coating thickness and to detect oxidation damage. The correlations shown in Figures 10 and 11 indicate that the eddy current test is the most accurate way to measure coating thickness. LTV supplied a mean estimate close to the true value. GE measurements, on average, underestimated. Discussions with LTV indicated that their method includes a correction for the change in substrate conductivity as a result of the coating thermal cycle. This correction was not made in the GE measurements and is the most likely source of discrepancy. The LTV estimate showed a slightly wider scatter about the true value. This is explained by the fact that the LTV estimate was an average of several readings for the whole specimen; whereas, the GE data plotted was the local estimate corresponding to the location of the metallographic section.

The eddy current measurement after oxidation test showed a reduced signal consistent with erosion of substrate material. This could be very useful as an in-situ method to locate oxidation damage. The method is limited in that it would be very difficult to extract much information about the severity, depth, location, and extent of the damage, although multifrequency methods could give more information than the basic test described here.

10.3 X-RAY CT RESULTS

X-ray CT was evaluated for potential to measure coating thickness and oxidation damage. The maximum CT number (extracted as described in Section 3.4) produced a reasonable correlation with thickness, although not as good as that of the eddy current test. In spite of the accuracy limitation, the X-ray CT method has the great advantage of being an imaging method, and the cross-sectional images provide an excellent indication of thickness variations. There is considerable room for improvement in the method by which thickness is estimated from the CT image. More smoothing and averaging would almost certainly give a closer estimate than the peak number used here.

CT estimation of coating thickness on inhibited-matrix substrate would be a much more difficult problem. Figures 45 and 46 show that the materials are radiographically more dense and nonuniform, and the presence of coating produces very little radiographic contrast.

10.4 BETA BACKSCATTER AND THERMOGRAPHY

Beta backscatter measurements gave an estimate of coating thickness that was less accurate than the eddy current test. Considering the slowness of the method, it appears to offer no advantage for the LTV materials studied. There may be some application to inhibited-matrix substrates where variable substrate electrical conductivity could rule out the eddy current method.

The thermographic method was explored in a very limited range of tests. Results indicated the method offers some ability to detect underlying damage. More work is needed to assess the capability and limitations of this method.

10.5 STATUS AND FUTURE DIRECTIONS

There are a number of satisfactory NDE methods for coated carbon-carbon with noninhibited matrix. The uniformity of the substrate density, chemical composition, and electrical conductivity allow reliable measurements to be made by X-ray CT and by eddy current. Additional methods such as beta back-scatter are available but not essential. There is no good method to assess directly the oxidation-protective ability of the coating although oxidation damage can be detected and characterized nondestructively at an early stage.

The situation for inhibited-matrix carbon-carbon is entirely different. The nonuniformity of the substrate renders every NDE method more difficult. This is complicated by the fact that materials and processes are not yet defined, so reliable materials-property values cannot be established. Because the newer coatings are multilayered, NDE methods would ideally characterize individual layers in the coating, a much more stringent requirement than for the conversion coatings. As this type of material offers the highest perform-ance, primary development effort should be in developing NDE methods for coated, inhibited-matrix materials.

REFERENCES

1. Koenig, J.R., "Mechanical, Thermal and Nondestructive Evaluation of Six Exit Cones in Support of the Scan Criteria Program," SoRI Final Report to Boeing Aerospace Corp under Boeing Aerospace Contract GN3166 (in support of Prime Contract F04701-78-C-0040), 1987.

2. Segal, E., Notea, A., and Segal, Y, "Dimensional Information Through Industrial Computerized Tomography," Materials Evaluation, Vol 40 (1982) pp 1268-1272.

3. Olden, J.T. and Rippenberger, Mechanics of Elastic Structures, McGraw-Hill, 1983.

END

DATE

FILMED

APRIL

1988

DTIC